Research Square

Preprints are preliminary reports that have not undergone peer review.
They should not be considered conclusive, used to inform clinical practice,
or referenced by the media as validated information.

Numerical Investigation of Hydrothermal Characteristics in a Darcy-Forchheimer Porous Channel: Influence of Partial Nanofluid Injection and Thermal Dispersion using Buongiorno's Model

Amir Basiri Parsa

amirbparsa@hut.ac.ir

Hamedan University of Technology

Habib-Olah. Sayehvand

Bu-Ali Sina University

Research Article

Keywords: Brinkman porous channel, Brownian motion, Buongiorno model, Nanofluid, Numerical solution, Partial nanofluid injection, Thermal dispersion

Posted Date: August 27th, 2026

DOI: https://doi.org/10.21203/rs.3.rs-10749541/v1

License: This work is licensed under a Creative Commons Attribution 4.0 International License.
Read Full License

Additional Declarations: No competing interests reported.

Numerical Investigation of Hydrothermal Characteristics in a Darcy-Forchheimer Porous Channel: Influence of Partial Nanofluid Injection and Thermal Dispersion using Buongiorno's Model

Amir Basiri Parsa [1], Habib-Olah. Sayehvand [2],

[1] Department of Mechanical Engineering, Hamedan University of Technology, Hamedan, Iran

[2] Department of Mechanical Engineering, Engineering Faculty of Bu-Ali Sina University, Hamedan, Iran.

Abstract:

This study presents a comprehensive numerical simulation of the hydrothermal behavior of nanofluid flow within a horizontal channel saturated with a Darcy-Forchheimer porous medium. Unlike simplified models that rely on Ordinary Differential Equations (ODEs), this work solves the full system of governing non-linear Partial Differential Equations (PDEs) to capture the complete evolution of the flow field. The nanofluid is modeled using Buongiorno's non-homogeneous two-phase framework, which accounts for Brownian motion and thermophoresis slip mechanisms. The numerical solution is implemented via the SIMPLER algorithm within a customized Fortran environment on a structured staggered grid. A primary novelty of this research is the investigation of partial nanoparticle injection at the boundary layers and its interaction with thermal dispersion effects. The results indicate that the local Nusselt and Sherwood numbers are significantly influenced by the injection thickness; however, an asymptotic behavior is observed where increasing the injection layer beyond a certain threshold yields negligible improvements in hydrothermal performance. Furthermore, it is found that elevating the thermal dispersion coefficient enhances lateral heat transport, thus intensifying the convective heat transfer rate. The results also indicate that among the investigated nanoparticles (Cu, Al_2O_3 and TiO_2), the Cu-water nanofluid exhibits the highest Nusselt number due to its superior thermal conductivity. This research provides a precise numerical tool and physical insights for optimizing porous media based cooling systems through strategic, partial nanofluid injection.

Key words: *Brinkman porous channel; Brownian motion; Buongiorno model; Nanofluid; Numerical solution; Partial nanofluid injection; Thermal dispersion.*

Nomenclature	
A	Cross-sectional area
a	Channel half-height
C_F	Forchheimer coefficient (Inertial resistance factor)
c_p	specific heat at constant pressure
C^*	thermal dispersion coefficient
D_B	Brownian diffusion coefficient
D_T	thermal diffusion coefficient
Da	Darcy number
d_p	nanoparticle diameter
h	average wall heat transfer coefficient
k	thermal conductivity
K	permeability
L^*, L	dimensionless and dimensional channel length
$\dot{m}$	mass flow rate
N_B	Brownian motion parameter
N_T	thermophoresis parameter
Nu	Nusselt number
P, p	dimensionless and dimensional pressure
Pr	Prandtl number
Re	Reynolds number
S, s	dimensionless and dimensional nanofluid injection thickness
Sc	Schmidt number
Sh	Sherwood number
T	temperature
U, u	dimensionless and dimensional axial velocities
V, v	dimensionless and dimensional Transverse velocities
$\bar{u}$	uniform axial velocity at the inlet
$\vec{V}_D$	Darcy velocity vector
X, x	dimensionless and dimensional axial coordinates
Y, y	dimensionless and dimensional normal coordinates
Greek letters	
α	Thermal diffusivity
ε	porosity
Φ, ϕ	dimensionless and dimensional nanoparticles volume fraction or concentration
μ	dynamic viscosity
θ	dimensionless temperature

ρ	density
v	kinematics viscosity
Subscript, Superscript	
f	fluid
eff	effective
i, in	inlet
m	mean quantity
nf	nanofluid
out	outlet
p	particles
w	wall

1. Introduction

Nanofluids, defined as suspensions of nanoscale particles (1-100 nm) in conventional base fluids, have emerged as promising candidates for advanced heat transfer applications. Their unique thermophysical properties have attracted attention across diverse fields such as thermal engineering, energy systems, electronics cooling, and biomedical processes. The concept of nanofluids was first introduced by Choi [1] in 1995, highlighting the potential of nanoparticles to enhance the effective thermal conductivity of otherwise low-conductivity base fluids. Subsequent studies confirmed that metallic nanoparticles (e.g., Cu, Ag) and metal oxides (e.g., Al_2O_3, CuO) can significantly improve the thermal performance of fluids when properly dispersed. Previous investigations have consistently demonstrated that even a small addition of nanoparticles can lead to a noticeable rise in the thermal conductivity of base fluids. Eastman et al. [2] reported that dispersing only 5% volume fraction of Al_2O_3, CuO, or Cu nanoparticles resulted in nearly 60% improvement in the effective conductivity of nanofluids. Several other studies have likewise confirmed that remarkable enhancements can be achieved at relatively low particle concentrations. A major advancement in nanofluid modeling was achieved by Buongiorno [3], who proposed a comprehensive framework for convective transport by

incorporating slip mechanisms between nanoparticles and the base fluid. Among the seven slip effects considered, Brownian diffusion and thermophoresis were identified as the dominant contributors to nanoparticle migration and heat transfer enhancement. This formulation provided a more realistic description compared to earlier homogeneous models such as Tiwari-Das [4], and has since become a cornerstone in nanofluid research. Subsequent investigations confirmed that nanoparticle transport phenomena strongly influence velocity and temperature fields, thereby affecting the overall heat transfer performance [5–7]. Recent investigations have expanded the application of Buongiorno's model to complex flow configurations. For example, Fetecau et al. [8] analyzed natural convection of nanofluids near an isothermal moving surface, while Bhatti and Rashidi [9] explored Brownian and thermophoretic effects in non-Newtonian nanofluid flows induced by stretching geometries. These studies underline the importance of nanoparticle transport phenomena in determining the overall heat transfer performance of nanofluids. As highlighted by Khaled and Vafaei [10], adjusting the distribution of dispersive elements such as nanoparticles or flexible fins within channel flows can enhance heat transfer, with boundary and exponential arrangements resulting in up to 21% improvement compared to uniform configurations and pointing toward the development of advanced nanofluids with superior cooling capabilities, while the nanofluid is modeled as a single-phase continuum with spatially varying effective thermal conductivity and a prescribed fully developed velocity profile rather than by solving the full momentum equations within a Buongiorno-type two-phase slip framework. Mousavi et al. [11] address the challenge of sustaining heat transfer performance in geothermal energy systems by systematically formulating and characterizing aluminum-water nanofluids stabilized with different surfactants (sodium dodecyl sulfate, Span 80, and (3-aminopropyl) triethoxysilane), combining an extensive suite of experimental techniques (scanning electron microscopy, ultraviolet-visible spectrometry, thermogravimetric analysis, dynamic light scattering, Fourier-transform infrared spectroscopy, turbidity, viscosity and density

measurements, computed tomography, and computational fluid dynamics with finite element method analysis) to show that properly surface-modified nanofluids can simultaneously improve thermal transport and reduce frictional losses -yielding up to about 30% higher energy recovery than water and roughly 12% gain over unmodified nanofluids- while a newly proposed stability index provides a quantitative framework for screening long-term-stable formulations for geothermal applications. A 41.9 percent thermal conductivity enhancement in Al-Cu/water hybrid nanofluids, as revealed by He et al. [12], stems from molecular dynamics insights into solid-like interfacial ordering and synergistic hydrogen bond-nanoparticle vibrational coupling at the optimal 40:60 ratio. Investigating the intricate interplay of convective boundary conditions and nonlinear stratification in nanofluid transport, Khan et al. [13] develop a comprehensive model for cubic doubly stratified rotating Casson nanofluid flow over an inclined bidirectional stretching sheet, incorporating mixed convection, velocity slip, Darcy/non-Darcy porous media, oblique magnetic fields, thermal radiation, viscous dissipation, heat generation/absorption, Brownian diffusion, and thermophoresis, with numerical solutions via Mathematica's NDSolve revealing that magnetic/Darcy effects suppress velocities while Biot numbers and radiation enhance temperature profiles for optimized heat/mass transfer in applications like semiconductor manufacturing and solar collectors.

Recent investigations have extended Buongiorno’s nanofluid framework to diverse physical situations. Shi et al. [14] and with Hayat et al. [15] focused on microorganism motility in non-Newtonian environments, where activation energy, radiative heat flux, and viscous dissipation were shown to play a decisive role in transport processes. In another work, Chu et al. [16] examined the Buongiorno problem under magnetohydrodynamic (MHD) influences and activation energy conditions, while also incorporating microbial motion into the fluid dynamics. Qasim et al. [17] investigated thin film nanofluid flow above an unsteady stretching sheet, employing Buongiorno’s formulation to capture heat and mass transfer characteristics. Nadeem et al. [18] presented a

parametric study where velocity, temperature, and concentration profiles were analyzed, with graphical results clarifying the sensitivity of thermal behavior to physical parameters. Rosca et al. [19] explored boundary layer flow and thermal transport over a permeable isothermal surface subject to stretching and shrinking, considering both nanofluid and hybrid nanofluid cases. Their work introduced a modified Buongiorno-type model to account for hybrid effects. In their recent work, Adnan et al. [20] analyzed Buongiorno nanofluid flow in thermally radiated inclined microchannels with microbial activity, showing that rotation and thermophoretic deposition enhance transport performance, whereas radiation effects reduce efficiency. Raja et al. [21] presented a numerical investigation of Buongiorno nanofluid flow over a stretching sheet using Al_2O_3, Cu, Ag, and TiO_2 nanoparticles, and concluded that variations in Brownian motion, thermophoresis, and particle fraction substantially reshape velocity, temperature, and concentration fields, ultimately enhancing heat transfer efficiency. Nihaal and Mahabaleshwar [22] studied hybrid nanofluid flow of TiO_2-Fe_2O_4 over a rotating cylinder in porous media, showing that porous resistance increases drag, thermophoresis reduces heat transfer, while Brownian motion enhances mass transport. Rahman et al. [23] developed a hybrid nanofluid model with graphene and Fe_2O_4 nanoparticles in channels with expanding/contracting walls, showing that nanoparticle fraction, Joule heating, and magnetic effects significantly alter density, thermal conductivity, and velocity distributions. By examining Cu-Al_2O_3/water hybrid nanofluid alongside conventional Cu/water nanofluid, Devi and Devi [24] revealed that hybrid formulations achieve higher heat transfer rates under Newtonian heating on a three-dimensional stretching surface, even in magnetohydrodynamic settings, with adjustable nanoparticle ratios offering further optimization. Rana et al. [25] analyzed electrically conducting alumina-water nanofluid flow over a horizontally shrinking cylinder with velocity and thermal slip, employing Buongiorno's non-homogeneous model together with nanolayer conductivity and Nielsen's viscosity formulations; their numerical results revealed that higher nanoparticle

concentration increases skin friction and Nusselt number, while larger particle diameters reduce heat transfer, with dual solution branches appearing under specific suction, curvature, and shrinking conditions. Several studies have employed Buongiorno's model to analyze diverse flow and heat transfer scenarios, including stretching sheets, rotating cylinders, porous media, and thermally radiated channels [26–46].

Building upon Darcy's classical description of porous flow, Forchheimer introduced an additional inertial correction that enables accurate representation of high-speed regimes [47]. Subsequent investigations, including those by Dero et al. [48], confirmed the relevance of this extended formulation at larger Reynolds numbers. Unlike the linear Darcy relation, the Darcy-Forchheimer framework incorporates a nonlinear resistance term, making it suitable for diverse engineering applications ranging from petroleum extraction and aquifer treatment to solar energy devices, reservoir engineering, thermal storage, and propulsion systems [49–58]. More recent contributions include investigations of Darcy-Forchheimer magnetohydrodynamic flow over variable-thickness stretchable sheets, incorporating chemical reactivity and heat generation effects, which demonstrate its relevance in aerodynamic structures, energy systems, and cooling technologies [59]. In addition, Darcy-Forchheimer Maxwell-MHD bio-convection nanofluid flow through a porous rotating disk, with entropy generation, thermal radiation, and chemical reactivity effects, has been analyzed using both analytical (HAM) and numerical (Bvp4c) approaches, highlighting its importance in gas turbines, braking systems, and glass manufacturing [60].

The mathematical formulation addresses boundary-layer motion of a Newtonian fluid over an extensible surface situated within a porous region beyond the classical Darcy description, where the added nonlinearity stems from the Forchheimer velocity-squared resistance rather than convective contributions. In related work, Khan et al. [61] examined micropolar ferrofluid transport in Darcy-Forchheimer porous structures while incorporating Joule heating and viscous dissipation effects.

Rasool et al. [62] presented an analysis of nanofluid transport governed by Darcy-Forchheimer magnetohydrodynamic effects along a nonlinear extensible surface. Darcy-Forchheimer modeling of tri-hybrid nanofluids, formulated with blood as the carrier medium and metallic/ceramic nanoparticles, has been explored in porous channels to illustrate potential biomedical applications such as targeted drug delivery, hyperthermia treatment, and magnetic endoscopy [63]. Gul et al. [64] investigated magnetohydrodynamic influences on the motion of three different tri-hybrid nanofluids over an elongated cylindrical surface. Power-law hybrid nanofluids over stretching surfaces are modeled by Endalew and Zhang [65], integrating inclined magnetic fields, Navier slip boundaries, and modified Fourier heat conduction; numerical solutions confirm superior surface heat transfer rates versus conventional nanofluids despite velocity suppression effects. Two-dimensional magnetohydrodynamic micropolar nanofluid flow over a stretching sheet is examined by Mittal and Kori [66], incorporating Brownian motion, thermophoresis, Darcy-Forchheimer porous resistance, chemical reaction, and thermal radiation with active/passive nanoparticle control; semi-analytical Homotopy Analysis Method solutions show magnetic and slip effects suppress velocity/microrotation while stretching rate and volume fraction enhance them for microscale heat/mass transfer applications. Velocity enhancement and reduced temperature/concentration in Reiner-Philippoff nanofluid flow over nonlinear stretching sheets are demonstrated by Ghoneim et al. [67], where Darcy-Forchheimer porosity, slip velocity, thermal radiation, activation energy, and Buongiorno effects with viscous dissipation collectively boost mass transfer for groundwater remediation applications. Also Hayat Khan et al. [68] examine time-fractional entropy generation in mixed convection of reacting nanofluids within Darcy-Forchheimer porous channels, integrating thermophoresis, buoyancy, chemical reactions, viscous dissipation, Brownian motion, and velocity slip; Euler wavelets with implicit differencing reveal that higher Eckert and Reynolds numbers boost entropy by 15-20 percent while pressure gradients and Forchheimer effects reduce it by 12 percent

for optimized porous media designs. Recent studies have examined melting effects in Darcy-Forchheimer porous media with nanofluid flow towards cylindrical surfaces under MHD stagnation-point conditions. Using the Buongiorno nanofluid model and numerical techniques, the influence of melting, curvature, magnetic field, and Brownian motion on velocity, temperature, and nanoparticle concentration has been reported, with results validated against existing data [69]. Darcy-Forchheimer thin-film flow of couple stress nanofluid with Manganese zinc ferrite and Graphene nanoparticles exhibits enhanced heat transfer under nonlinear thermal radiation, melting heat, and Newtonian heating, where Khemiri et al. [70] apply Adam-Bashforth predictor-corrector solutions to reveal that Darcy-Forchheimer resistance opposes flow while hybrid nanomaterials boost thermal performance for coating and microelectronics cooling applications. Asif Memonet al. [71] analyze dual solutions for Copper-Molybdenum disulfide micropolar water-based hybrid nanofluid boundary layer flow over stretching/shrinking surfaces under Darcy-Forchheimer porous resistance, thermal radiation, and partial slip, revealing that nanoparticle volume fractions boost Sherwood numbers while suppressing skin friction and Nusselt numbers amid suction and magnetic effects.

The main purpose of this study is to analyze the effects of partial nanoparticle injection (boundary arrangements) with varying thicknesses in a Darcy-Forchheimer porous channel using the most precise Buongiorno two-phase model. The fully coupled system of non-linear partial differential equations is solved numerically using a control volume method based on the SIMPLER algorithm. This approach accounts for thermal dispersion and non-uniform velocity, temperature, and concentration profiles, covering the entire flow development from the inlet to the fully developed conditions. The authors believe that the present study is new and innovative. The governing partial differential equations are transformed into dimensionless form and numerically solved using the control volume approach with SIMPLER algorithm. Graphical and tabular analysis reveals the effects of different physical parameters including nanoparticle arrangement type, injection zone thickness,

nanoparticle material, volume fraction, Reynolds number, and entrance/development region effects. In the present work, non-uniform two-phase nanofluid flow with precise thermal dispersion modeling is taken into account which covers many directions of nanofluid transport rarely considered by researchers in such porous channel studies. It is hoped that this article will prove helpful to new researchers working on advanced nanofluid applications, particularly those investigating optimal nanoparticle distribution strategies for heat transfer enhancement.

2. Flow Analysis and Mathematical Formulation

The steady, two-dimensional flow of a Newtonian, incompressible viscous nanofluid through a channel saturated with a porous medium is considered. The channel is formed by two parallel impermeable plates separated by a distance $2a$, and the porous region is assumed to be fully saturated with known properties. At the inlet section, a developing region of length l_1 exists. This is followed by a downstream region of length l_2 in which the flow and thermal fields are fully developed. As illustrated in **Fig. 1**, the x-axis is aligned with the channel centerline in the axial direction, while the y-axis is taken perpendicular to it. The fluid entering the channel may consist of pure fluid in part of the inlet cross-section and nanofluid (pure fluid with suspended nanoparticles) in another part. The fluid is assumed Newtonian, with thermophysical properties varying according to the local nanoparticle concentration. Both channel walls are maintained at a constant temperature T_w throughout the flow domain. Different configurations for nanoparticle injection at the channel inlet cross-section are considered. In one arrangement, referred to as boundary injection and illustrated in **Fig. 1**, nanoparticles are introduced into regions of thickness s adjacent to the channel walls, with a prescribed volume fraction ϕ_i relative to the base fluid.

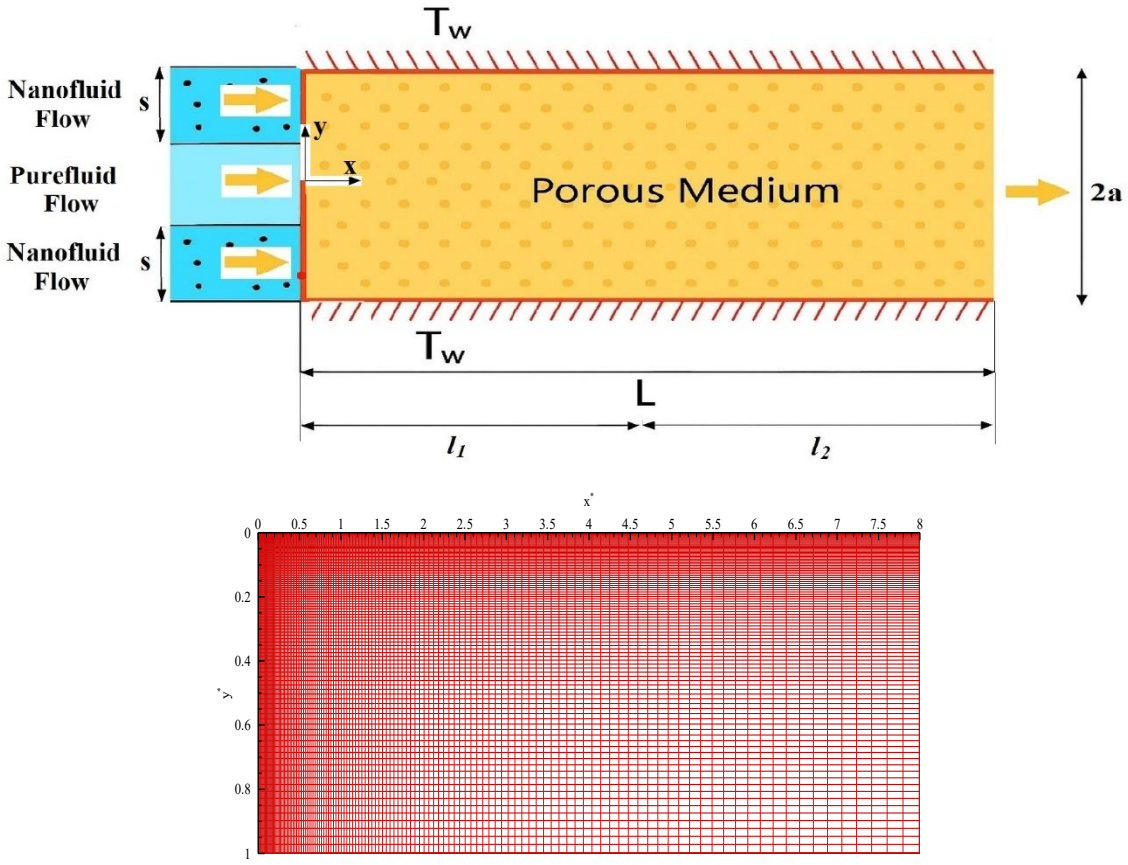


Fig. 1. The schematic of the problem and grid system.

As the flow proceeds in the axial direction, the nanoparticles gradually disperse throughout the entire channel. According to most previous studies, the porous medium is assumed to be homogeneous, isotropic, and in local thermal equilibrium with the fluid [72]. In addition, the effective properties of the porous medium are considered constant, whereas the thermophysical properties of the nanofluid vary depending on the nanoparticle concentration in different regions of the field [3]. Due to the preceding discussion and given the specific practical conditions of such problems, the steady-state solution is desired, and all time-dependent terms are neglected in the governing equations. Accordingly, the governing equations are considered in a two-dimensional (axisymmetric) and steady-state form. To prepare the equations for a clearer and more tractable numerical solution, they are nondimensionalized through the introduction of appropriate parameters. Assuming two-dimensional flow, the Darcy velocity vector is defined as $\vec{V}_D = u\,\hat{i} + v\,\hat{j}$ where $\hat{i}$ and $\hat{j}$ are unit

vectors in the axial and transverse directions of the channel, respectively. Under these assumptions, the conservation equations for nanofluid flow, including continuity, momentum, energy, and concentration, with the volumetric averaging notation omitted, are expressed as follows [3,72,73]:

$$\frac{\partial u}{\partial x}+\frac{\partial v}{\partial y}=0, \tag{1}$$

$$\begin{aligned}\frac{\rho_{nf}}{\varepsilon}\left[u\frac{\partial u}{\partial x}+v\frac{\partial u}{\partial y}\right]=&-\frac{\partial p^{nf}}{\partial x}+\frac{1}{\varepsilon}\left[\frac{\partial}{\partial x}\left(2\mu_{nf}\frac{\partial u}{\partial x}\right)+\frac{\partial}{\partial y}\left(\mu_{nf}(\frac{\partial u}{\partial y}+\frac{\partial v}{\partial x})\right)\right]-(\frac{\mu_{nf}}{K})u\\&-\frac{C_F}{\sqrt{K}}\rho_{nf}\left|\vec{V}_D\right|u,\end{aligned} \tag{2}$$

$$\begin{aligned}\frac{\rho_{nf}}{\varepsilon}\left[u\frac{\partial v}{\partial x}+v\frac{\partial v}{\partial y}\right]=&-\frac{\partial p^{nf}}{\partial y}+\frac{1}{\varepsilon}\left[\frac{\partial}{\partial x}\left(\mu_{nf}(\frac{\partial u}{\partial y}+\frac{\partial v}{\partial x})\right)+\frac{\partial}{\partial y}\left(2\mu_{nf}\frac{\partial v}{\partial y}\right)\right]-(\frac{\mu_{nf}}{K})v\\&-\frac{C_F}{\sqrt{K}}\rho_{nf}\left|\vec{V}_D\right|v,\end{aligned} \tag{3}$$

$$\begin{aligned}\rho_{nf}\left[u\frac{\partial c_{p_{nf}}T}{\partial x}+v\frac{\partial c_{p_{nf}}T}{\partial y}\right]=&\frac{\partial}{\partial x}\left[k_{eff}(\frac{\partial T}{\partial x}+\frac{\partial T}{\partial y})\right]\\&+\varepsilon(\rho c_p)_p\left[D_B\left(\frac{\partial\phi}{\partial x}\frac{\partial T}{\partial x}+\frac{\partial\phi}{\partial y}\frac{\partial T}{\partial y}\right)+\frac{D_T}{T_w}\left(\left(\frac{\partial T}{\partial x}\right)^2+\left(\frac{\partial T}{\partial y}\right)^2\right)\right].\end{aligned} \tag{4}$$

$$\frac{1}{\varepsilon}\left[u\frac{\partial\phi}{\partial x}+v\frac{\partial\phi}{\partial y}\right]=D_B\left(\frac{\partial^2\phi}{\partial x^2}+\frac{\partial^2\phi}{\partial y^2}\right)+\frac{D_T}{T_w}\left(\frac{\partial^2 T}{\partial x^2}+\frac{\partial^2 T}{\partial y^2}\right). \tag{5}$$

For the pressure gradient terms in Eqs. (2) and (3), based on the volume-averaging method and the assumption of constant porosity, one can write [42, 132, 133]: $\nabla\langle p\rangle^{nf}=\nabla\langle p\rangle/\varepsilon$, where p denotes the effective nanofluid pressure inside the channel. Since the coefficients D_B and D_T depend respectively on temperature and local nanoparticle concentration, and given the limited variation of these parameters, average values within the channel are adopted. Accordingly, the coefficients D_B and D_T are treated as constants to facilitate appropriate nondimensionalization. Also, in the governing equations, k_{eff} denotes the effective thermal conductivity of the porous medium, which

combines the stagnant nanofluid conductivity with the additional contribution from thermal dispersion. A detailed analysis of this formulation is presented in the subsequent section.

The boundary conditions of the problem, consistent with the geometry and practical features, are defined as follows:

- **Inlet:** A uniform axial velocity $\bar{u}$ (with zero transverse component) and a uniform inlet temperature T_i are imposed. For nanoparticle concentration, partial injection is considered: in part of the inlet cross-section, nanoparticles enter with a uniform volume fraction ϕ_i, while the remaining section admits pure base fluid.
- **Walls:** No-slip condition is applied, i.e., both axial and transverse velocity components vanish at the walls. A constant wall temperature T_w is prescribed. For nanoparticle concentration, a physically consistent condition is adopted: the net nanoparticle flux at the wall is set to zero, implying no deposition or generation. This leads to a Robin-type boundary condition as: $D_B \frac{\partial \phi}{\partial y}\Big|_{y=a} = -\frac{D_T}{T_w}\frac{\partial T}{\partial y}\Big|_{y=a}$, while the longitudinal concentration gradient at the wall is assumed zero.
- **Centerline:** Due to symmetry, zero-gradient conditions are imposed for all variables along the channel centerline, allowing half-domain computation.
- **Outlet:** No explicit boundary condition is required. Numerical extrapolation is applied at the downstream boundary, consistent with the finite volume SIMPLE algorithm. For sufficiently high Péclet numbers, the outlet behaves as a convective boundary, and developed flow conditions for velocity and temperature are assumed. For nanoparticle concentration, linear extrapolation of neighboring nodes is used. Mass conservation of the nanofluid (equal inlet and outlet mass flow rate) is enforced at each iteration to ensure convergence.

Based on the above discussion, the boundary conditions of the problem are mathematically formulated as follows:

Inlet:

$$\begin{aligned} &u(0,y)=\bar{u},\ \ v(0,y)=0,\\ &T(0,y)=T_i, \end{aligned} \tag{6}$$

$$\phi(0,y)=\begin{cases} 0 & 0<y<s \\ \phi_i & s<y<a \end{cases}$$

Walls:

$$\begin{aligned} &u(x,a)=0,\ \ v(x,a)=0,\\ &T(x,a)=T_w, \end{aligned} \tag{7}$$

$$\frac{\partial\phi(x,a)}{\partial y}=-\frac{D_T}{T_w D_B}\left(\frac{\partial T(x,a)}{\partial y}\right).$$

Centerline:

$$\begin{aligned} &\frac{\partial u(x,0)}{\partial y}=0,\ \ \frac{\partial v(x,0)}{\partial y}=0,\\ &\frac{\partial T(x,0)}{\partial y}=0,\\ &\frac{\partial\phi(x,0)}{\partial y}=0. \end{aligned} \tag{8}$$

Outlet (For faster convergence):

$$\dot{m}_{out}=\dot{m}_{in},\ \ \int_0^a\left(\rho u(L,y)\,dA\right)_{out}=\int_0^a\left(\rho u(0,y)\,dA\right)_{in} \tag{9}$$

Understanding transport mechanisms in nanofluids requires expressing the governing equations in nondimensional and conservative forms.

$$X \equiv \frac{x}{a},\ \Phi \equiv \frac{\phi}{\phi_i},\ \theta \equiv \frac{T-T_i}{T_w-T_i},\ P \equiv \frac{p}{\rho_f \bar{u}^2},\ V \equiv \frac{v}{\bar{u}},\ U \equiv \frac{u}{\bar{u}},\ L^* \equiv \frac{L}{a},\ S \equiv \frac{s}{a},\ Y \equiv \frac{y}{a},$$

$$\mathrm{Re} = \frac{2a\rho_f \bar{u}}{\mu_f},\ \mathrm{Pr} = \frac{\nu_f}{\alpha_f} = \frac{\mu_f c_{p_f}}{k_f},\ Da = \frac{K}{a^2} \tag{10}$$

$$N_B = \frac{(\rho c_p)_p}{(\rho c_p)_f}\frac{D_B \phi_i}{\alpha_f},\quad N_T = \frac{(\rho c_p)_p}{(\rho c_p)_f}\frac{D_T (T_w - T_i)}{\alpha_f T_w},\ Sc = \frac{\mu_f}{\rho_f D_B}$$

Each dimensionless quantity is defined with respect to its corresponding reference value. By substituting these nondimensional variables into the conservation equations (1)-(5), the governing system is reformulated in dimensionless form:

$$\frac{\partial U}{\partial X} + \frac{\partial V}{\partial Y} = 0, \tag{11}$$

$$\frac{\rho_{nf}}{\rho_f}\left[U\frac{\partial U}{\partial X} + V\frac{\partial U}{\partial Y}\right] = -\frac{\partial P}{\partial X} + \frac{2}{\mathrm{Re}}\frac{1}{\mu_f}\left[\begin{array}{l}\frac{\partial}{\partial X}\left(2\mu_{nf}\frac{\partial U}{\partial X}\right)+\\ \frac{\partial}{\partial Y}\left(\mu_{nf}\left(\frac{\partial U}{\partial Y}+\frac{\partial V}{\partial X}\right)\right)\end{array}\right] - \left[\frac{2\varepsilon}{Da.\mathrm{Re}}\frac{\mu_{nf}}{\mu_f} + \frac{\varepsilon C_F}{\sqrt{Da}}\frac{\rho_{nf}}{\rho_f}\left|\vec{V}_D\right|\right]U, \tag{12}$$

$$\frac{\rho_{nf}}{\rho_f}\left[U\frac{\partial V}{\partial X} + V\frac{\partial V}{\partial Y}\right] = -\frac{\partial P}{\partial Y} + \frac{2}{\mathrm{Re}}\frac{1}{\mu_f}\left[\begin{array}{l}\frac{\partial}{\partial X}\left(\mu_{nf}\left(\frac{\partial U}{\partial Y}+\frac{\partial V}{\partial X}\right)\right)+\\ \frac{\partial}{\partial Y}\left(2\mu_{nf}\frac{\partial V}{\partial Y}\right)\end{array}\right] - \left[\frac{2\varepsilon}{Da.\mathrm{Re}}\frac{\mu_{nf}}{\mu_f} + \frac{\varepsilon C_F}{\sqrt{Da}}\frac{\rho_{nf}}{\rho_f}\left|\vec{V}_D\right|\right]V, \tag{13}$$

$$\frac{\rho_{nf}}{(\rho c_p)_f}\left[U\frac{\partial c_{p_{nf}}\theta}{\partial X} + V\frac{\partial c_{p_{nf}}\theta}{\partial Y}\right] = \frac{2}{\mathrm{Re.Pr}}\frac{1}{k_f}\left[\frac{\partial}{\partial X}k_{eff}\frac{\partial \theta}{\partial X} + \frac{\partial}{\partial Y}k_{eff}\frac{\partial \theta}{\partial Y}\right] + \frac{2\varepsilon}{\mathrm{Re.Pr}}\left[N_B\left(\frac{\partial \Phi}{\partial X}\frac{\partial \theta}{\partial X} + \frac{\partial \Phi}{\partial Y}\frac{\partial \theta}{\partial Y}\right) + N_T\left(\left(\frac{\partial \theta}{\partial X}\right)^2 + \left(\frac{\partial \theta}{\partial Y}\right)^2\right)\right]. \tag{14}$$

$$\left[U\frac{\partial \Phi}{\partial X} + v\frac{\partial \Phi}{\partial Y}\right] = \frac{2\varepsilon}{\mathrm{Re}.Sc}\left[\left(\frac{\partial^2 \Phi}{\partial X^2} + \frac{\partial^2 \Phi}{\partial Y^2}\right) + \frac{N_T}{N_B}\left(\frac{\partial^2 \theta}{\partial X^2} + \frac{\partial^2 \theta}{\partial Y^2}\right)\right]. \tag{15}$$

In Eqs. (12) and (13), $\left|\vec{V}_D\right|$ represents the magnitude of the local dimensionless velocity vector. As previously mentioned, it is defined as $\left|\vec{V}_D\right| = \sqrt{U^2 + V^2}$, which accounts for the non-linear Forchheimer resistance within the porous medium. This term, along with the Darcy term, characterizes the total pressure drop across the porous structure.

The dimensionless boundary conditions:

$$\begin{aligned} &U(0,Y) = 1, \;\; V(0,Y) = 0, \\ &\theta(0,Y) = 0, \\ &\Phi(0,Y) = \begin{cases} 0 & 0 < Y < S \\ 1 & S < Y < 1 \end{cases} \end{aligned} \tag{16}$$

$$\begin{aligned} &U(X,1) = 0, \;\; V(X,1) = 0, \\ &\theta(X,1) = 1, \\ &\frac{\partial \Phi(X,1)}{\partial Y} = -\frac{N_T}{N_B}\left(\frac{\partial \theta(X,1)}{\partial Y}\right). \end{aligned} \tag{17}$$

$$\begin{aligned} &\frac{\partial U(X,0)}{\partial Y} = 0, \;\; \frac{\partial V(X,0)}{\partial Y} = 0, \\ &\frac{\partial \theta(X,0)}{\partial Y} = 0, \\ &\frac{\partial \Phi(X,0)}{\partial Y} = 0. \end{aligned} \tag{18}$$

$$\int_0^1 \left(\rho U(L^*,Y)dY\right)_{out} = \int_0^1 \left(\rho U(0,Y)dY\right)_{In} \tag{19}$$

The addition of nanoparticles to a base fluid alters its thermophysical properties, including thermal conductivity, viscosity, and specific heat, thereby influencing convective heat transfer. The final properties depend strongly on particle type, concentration, purity, shape, and size. Several empirical correlations have been proposed to describe these effects. Heat transfer enhancement in nanofluids can be explained by two mechanisms: (i) increased effective conductivity due to suspended nanoparticles, and (ii) thermal dispersion arising from the random motion of ultrafine particles. Consequently, the overall effective conductivity of a nanofluid (k_{nf}) is expressed as the

sum of the statics nanofluid conductivity (k_{Static}) and the contribution from thermal dispersion ($k_{Dispersion}$) [3,74]:

$$k_{nf} = k_{Static} + k_{Dispersion} \tag{20}$$

Experimental and theoretical studies confirm that nanoparticles enhance fluid thermal conductivity by forming interfacial thermal bridges. A modified Maxwell model with minimal error was later proposed by Wasp et al. [75]:

$$k_{Static} = k_f \left[\frac{k_p + 2k_f - 2(k_f - k_p)\phi}{k_p + 2k_f + 2(k_f - k_p)\phi} \right], \tag{21}$$

For thermal dispersion, the correlation proposed by Xu and Roetzel [76] is adopted as the preferred model for estimating the effective conductivity contribution:

$$k_{Dispersion} = C^*(\rho c_p)_{nf}\, \phi a u \tag{22}$$

Therefore:

$$k_{nf} = k_f \left[\frac{k_p + 2k_f - 2(k_f - k_p)\phi}{k_p + 2k_f + 2(k_f - k_p)\phi} \right] + C^*(\rho c_p)_{nf}\, \phi a u \tag{23}$$

Finally, the effect of the porous matrix on the overall thermal conductivity must be considered. Based on established correlations, the relation proposed by Nield and Bejan [77] is adopted, accounting for both the nanofluid flow and the porous medium properties:

$$\frac{1}{k_{eff}} = \frac{\varepsilon}{k_{nf}} + \frac{1-\varepsilon}{k_s} \tag{24}$$

The thermophysical properties of nanofluids, including specific heat, density, and dynamic viscosity, are calculated using the following model equations [78–80]:

$$\begin{aligned} c_{p_{nf}} &= \phi c_{p_p} + (1-\phi) c_{p_f} \\ \rho_{nf} &= \phi \rho_p + (1-\phi) \rho_f \end{aligned} \tag{25}$$

$$\mu_{nf} = \frac{\mu_f}{(1-\phi)^{2.5}},$$

The governing expressions for the relevant physical quantities are formulated as follows [81,82]:

$$Nu_X = 4\frac{k_{nf}}{k_f}\frac{\frac{\partial\theta}{\partial Y}\big|_{Y=1}}{(\theta_w-\theta_m)},\ \overline{Nu} = \frac{\int_0^L Nu_X dX}{L}.$$
$$Sh_X = 4\frac{\frac{\partial\Phi}{\partial Y}\big|_{Y=1}}{(\Phi_w-\Phi_m)},\ \overline{Sh} = \frac{\int_0^L Sh_X dX}{L}. \quad (26)$$

3. Numerical Method and Grid Convergence Study

The governing transport equations were discretized using the finite volume method on a structured grid. Pressure–velocity coupling was resolved through the **SIMPLER (Semi-Implicit Method for Pressure-Linked Equations Revised)** algorithm, which improves stability compared to the classical SIMPLE scheme.

The iterative cycle, schematically presented in **Fig. 2**, can be summarized as follows:

- Start with provisional distributions of velocity, pressure, and scalar variables.
- Compute pseudo-velocities from the discretized momentum equations without pressure correction.
- Solve the auxiliary pressure equation to refine the pressure field.
- Update velocity components using corrected pressure gradients.
- Enforce continuity by solving the pressure correction equation.
- Correct velocity and pressure fields, then advance scalar transport equations (temperature and nanoparticle concentration).
- Repeat until residuals of all governing equations fall below the prescribed tolerance.

Due to the nonlinear nature of the Forchheimer term in the momentum equation and the Brownian and thermophoretic contributions in the energy equation, a linearization procedure was required. Initial estimates for velocity, temperature, and nanoparticle concentration were assigned across all grid nodes. Nonlinear expressions were reformulated as products of known and unknown quantities to facilitate linearization. Once discretized, the system -together with the boundary conditions- was reduced to a tridiagonal matrix of algebraic equations, which was solved using Gaussian elimination to update the field variables in each iteration. This process was repeated until the solution converged within a predefined tolerance.

To ensure numerical robustness, a grid refinement analysis was conducted. Successive mesh refinements in both axial and transverse directions revealed that beyond a certain resolution, variations in velocity, temperature, and nanoparticle concentration profiles became negligible, confirming grid independence of the solution.

To reduce discretization errors and accurately resolve steep gradients of velocity, temperature, and nanoparticle concentration, a non-uniform computational mesh was generated with refined spacing near the channel walls and in the inlet region (see **Fig. 1**). Owing to the planar symmetry of the physical domain, only half of the channel cross-section was discretized.

The resulting mesh consisted of 101 nodes in the transverse direction and 91 nodes in the axial direction. A grid independence study was conducted to assess the sensitivity of the numerical solution to mesh resolution by analyzing the axial distribution of the local wall Nusselt number. Five different mesh configurations were examined, denoted as 31×41 91×101 ، 81×91 ، 45×55 and 121×141.

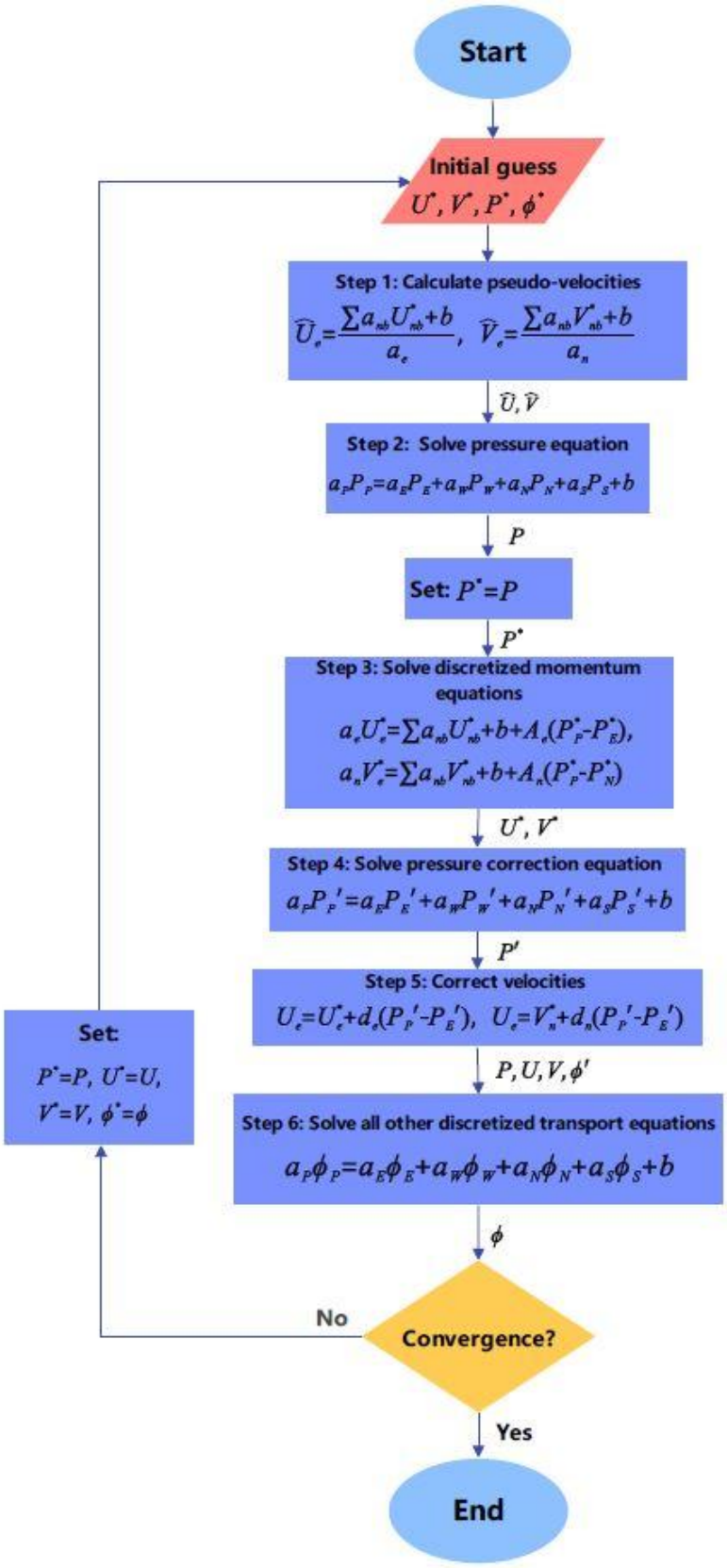


Fig. 2. The SIMPLER solution procedure.

To ensure numerical stability and to avoid large deviations in the velocity, temperature, and nanoparticle concentration fields near the inlet and close to the channel walls, mesh refinement was applied in both axial and transverse directions. Representative values of the governing physical parameters were selected for the grid sensitivity analysis. The axial variation of the wall Nusselt number for the different mesh resolutions under boundary nanoparticle injection conditions is shown in **Fig. 3**. As observed in **Fig. 3**, the solution obtained with the coarsest mesh exhibits significant inaccuracies and is therefore discarded. The intermediate meshes show noticeable deviations compared with the two finest grids. In contrast, the difference between the two finest mesh resolutions is negligible, indicating that grid convergence has been achieved. Consequently, the mesh with 91×101 nodes provides an optimal balance between accuracy and computational cost and is adopted for all subsequent numerical simulations.

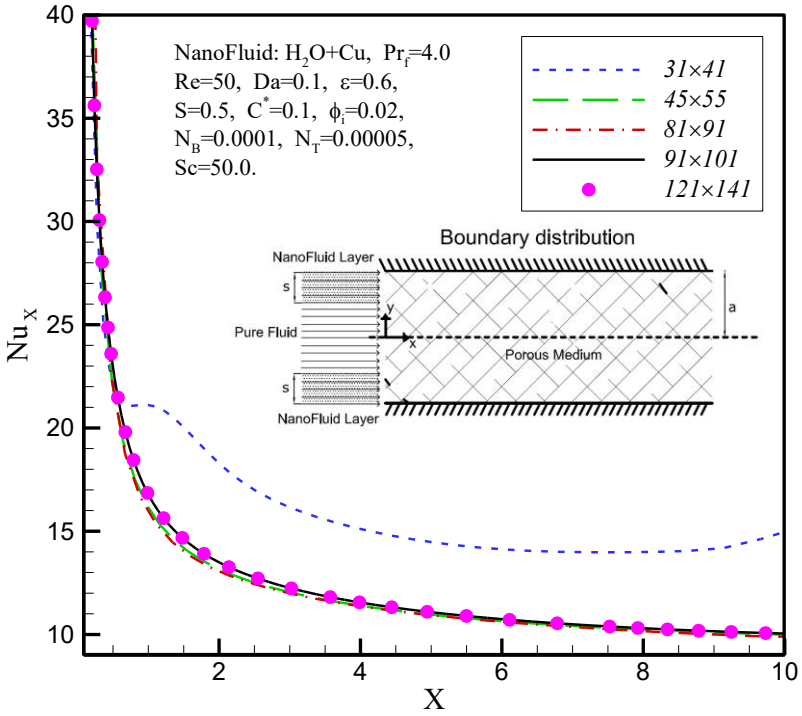


Fig. 3. Axial variation of the wall Nusselt number for different mesh resolutions (grid independence study).

The discrete algebraic equations are solved iteratively due to the nonlinear dependence of the coefficients on the unknown variables, particularly in the porous region. An initial guess is assigned

at all nodes, and the equations are repeatedly solved using the Thomas algorithm (tridiagonal matrix method) until convergence is achieved. **Fig. 4** shows the convergence history of the momentum equation for different Reynolds and Darcy numbers. About 35,000 iterations are sufficient under the most demanding conditions. Lower Darcy or Reynolds numbers require additional iterations to reach convergence.

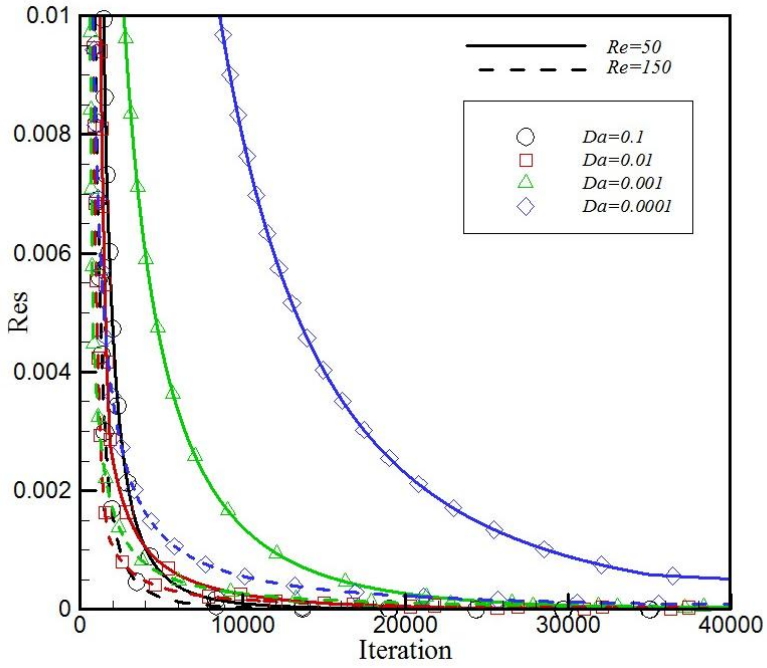


Fig. 4. Convergence of the momentum equation for different Reynolds and Darcy numbers.

4. Comparisons and verification

To ensure the accuracy of the present numerical method, the results are validated against experimental data reported by Fazeli et al. [83], who studied forced convection of Al_2O_3-water nanofluid in the entrance region of a two-dimensional channel. Their study combined experimental measurements with numerical simulations using a two-phase model without thermal dispersion. **Fig. 5** compares the local convective heat transfer coefficient along the channel wall predicted by the present two-phase Buongiorno model with their numerical and experimental results for inlet volume fractions of $\phi_i = 0.04$ and $\mathrm{Re} = 1588$. The Buongiorno model shows better agreement with

experimental data than the single-phase model, due to its realistic treatment of nanoparticle transport and inclusion of thermal dispersion. The model's accuracy improves at higher Reynolds numbers, where the influence of thermal dispersion on convective heat transfer becomes more significant.

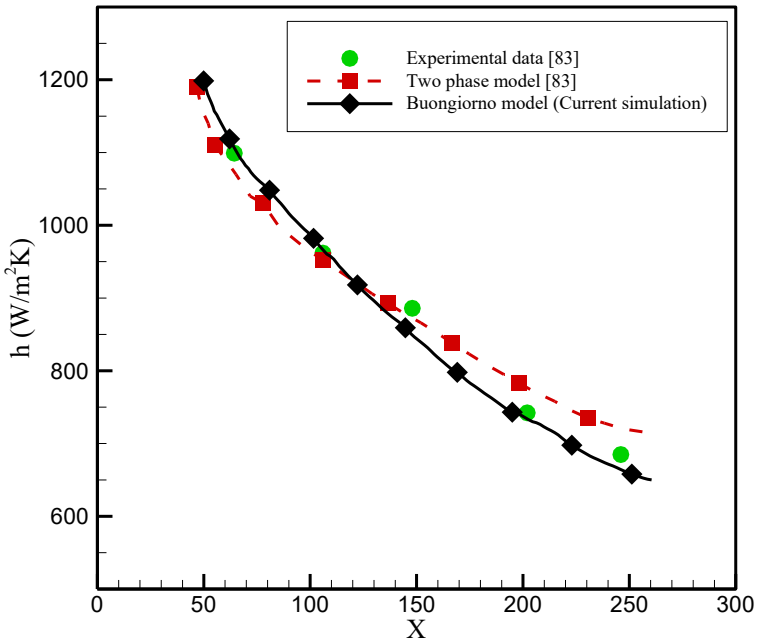


Fig. 5. Comparison of numerical results with experimental data and the two-phase model [83] for average wall heat transfer coefficient in the channel.

5. Results and Discussion

This section presents the numerical findings concerning the hydrothermal behavior and nanoparticle dispersion within the porous channel. The current numerical model utilizes the Brinkman-Forchheimer equations and a finite volume approach. To ensure the reliability of the computational framework, this model was validated against established empirical data and analytical solutions, showing excellent agreement. Following validation, the results delineate the intricate flow physics within the entry region, which are often neglected in simplified models despite their significant impact on heat transfer under varying Reynolds and Prandtl numbers. A key finding involves the efficiency of partial nanofluid injection. This study indicates that partial injection near

the boundaries or the channel centerline serves as a thermally effective and cost-effective alternative to complete saturation.

To further characterize these phenomena, a systematic parametric study was conducted to evaluate the influence of dimensionless variables, including the Reynolds (Re), Prandtl (Pr), Darcy (Da), and Schmidt (Sc) numbers, alongside porosity (ε) and nanoparticle injection thickness (S). By isolating the effects of Brownian motion (N_B) and thermophoresis (N_T) against the baseline values established in **Table 1**, the study highlights how the interplay between porous resistance and focused injection optimizes the local Nusselt number. Given that the porous matrix significantly accelerates flow development compared to clear channels, a longitudinal aspect ratio of $l/a = 10$ was maintained to ensure a transition to fully developed conditions at the exit. While both wall-based and centerline configurations were examined, the primary analysis focuses on a 50% boundary injection profile due to its superior thermal performance, particularly within the developing zone where gradient intensities are most pronounced.

Table 1. Baseline values for the governing dimensionless parameters.

Dimensionless Parameter	Symbol	Baseline Value
Reynolds number	Re	$\mathrm{Re} = 50$
Darcy number	Da	$Da = 0.1$
Porosity	ε	$\varepsilon = 0.6$
Injected layer thickness	S	$S = 0.5$
Thermal dispersion coefficient	C^*	$C^* = 0.1$
Injected nanoparticle volume fraction	ϕ_i	$\phi_i = 0.02$
Brownian motion parameter	N_B	$N_B = 0.001$
Thermophoresis parameter	N_T	$N_T = 0.00005$

Schmidt number	Sc	$Sc = 50.0$

To simulate realistic heat exchanger conditions, water was utilized as the base fluid with Cu ($d_p = 6\times10^{-11}\,m$) as the reference nanoparticle, while Al_2O_3 and TiO_2 were evaluated for comparative analysis. Thermophysical properties were determined at the mean temperature, assuming an inlet temperature of $T_i = 20^o C$ and a constant wall temperature of $T_w = 80^o C$. The porous domain consisted of silicon dioxide (SiO_2) with a fixed thermal conductivity of $k_s = 1.5 W/m.K$ [84]. **Tables 2 and 3** summarize the detailed thermophysical specifications for these materials.

Table 2. Thermophysical properties of the base fluid (water) at various temperatures [85].

Property	**Unit**	$T = 20^O C$	$T = 45^O C$	$T = 170^O C$	$T = 240^O C$
Density (ρ)	kg/m^3	998	999.1	890.2	818.3
Specific heat (c_p)	$J/kg.K$	4181	4179	4440	4740
Thermal conductivity (k)	$W/m.K$	0.606	0.634	0.678	0.631
Dynamic viscosity (μ)	$N.s/m^2$	0.000959	0.000631	0.000152	0.000113
Prandtl number (Pr)	-	6.62	4.0	1.0	0.85

Table 3. Thermophysical properties of the investigated nanoparticles [86].

Property	**Unit**	**Copper** (Cu)	**Alumina** (Al_2O_3)	**Titania** (TiO_2)
Density (ρ)	kg/m^3	8933	3970	4250
Specific heat (c_p)	$J/kg.K$	385	765	686.2
Thermal conductivity (k)	$W/m.K$	400	40	8.9

To establish a benchmark for subsequent parametric investigations, the fundamental hydrodynamic and thermal characteristics were evaluated using the reference properties specified in **Table 1**. The streamline distribution in **Fig. 6** confirms that the flow field is governed by axial momentum. Near the channel entrance, boundary-induced shear and wall friction cause a localized transverse deflection toward the centerline. The flow maintains a predominantly horizontal orientation and stabilizes into a parallel pattern further downstream. The nanoparticles are introduced

at the inlet via a partial boundary-layer injection with a 50% spatial distribution. This injection modifies local velocity magnitudes but has a negligible impact on the overall flow topology. The spatial development of the axial velocity profiles is further detailed in **Fig. 7**. This figure highlights the transition from a uniform inlet velocity at $X = 0$ to a fully developed state as the flow progresses along the channel. Based on the dimensionless channel length, it is evident that hydrodynamic development occurs before the final quarter of the channel. The results indicate that the hydrodynamic entry length is less than three-quarters of the total channel length.

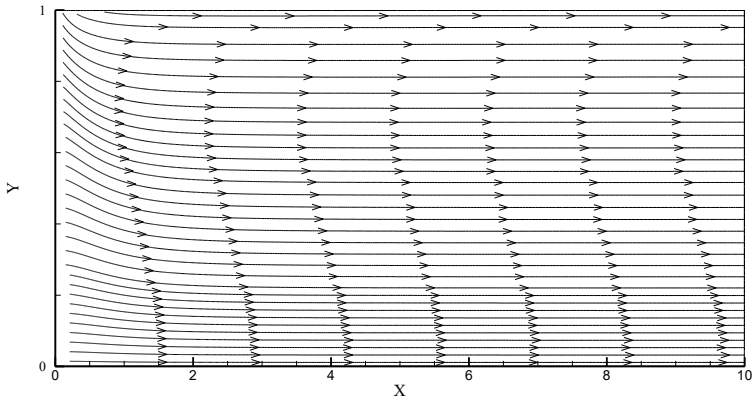


Fig. 6. Streamline distribution within the channel.

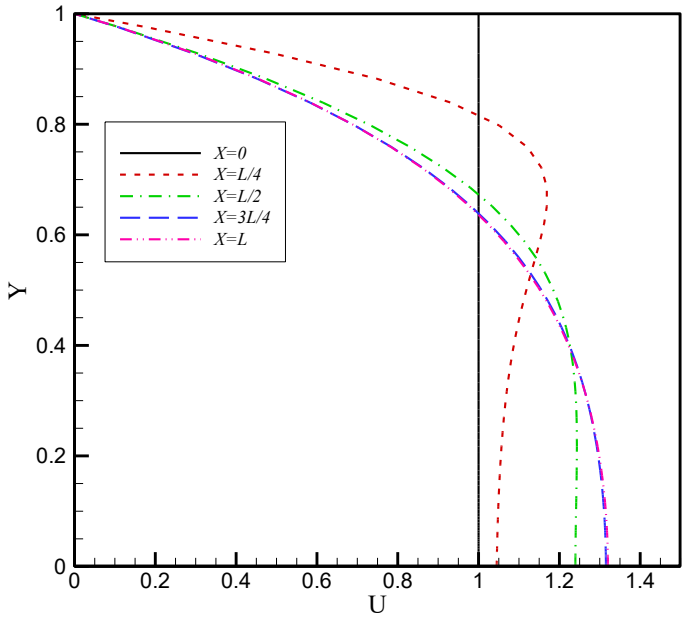


Fig. 7. Dimensionless axial velocity profiles at various longitudinal locations along the channel.

Fig. 8 illustrates the axial pressure and pressure gradient distributions along the channel centerline. Near the inlet, the pressure approximates the ambient injection value, with the initial drop driven by the combined effects of fluid acceleration and wall shear stress. At lower Reynolds numbers, viscous effects dominate the entry region, resulting in a consistent pressure decline. Further downstream, the pressure distribution decreases linearly with axial distance. The maximum pressure drop occurs near the entrance, while the pressure gradient stabilizes at a constant value in the fully developed region. The negative sign of the gradient reflects the continuous pressure loss along the channel.

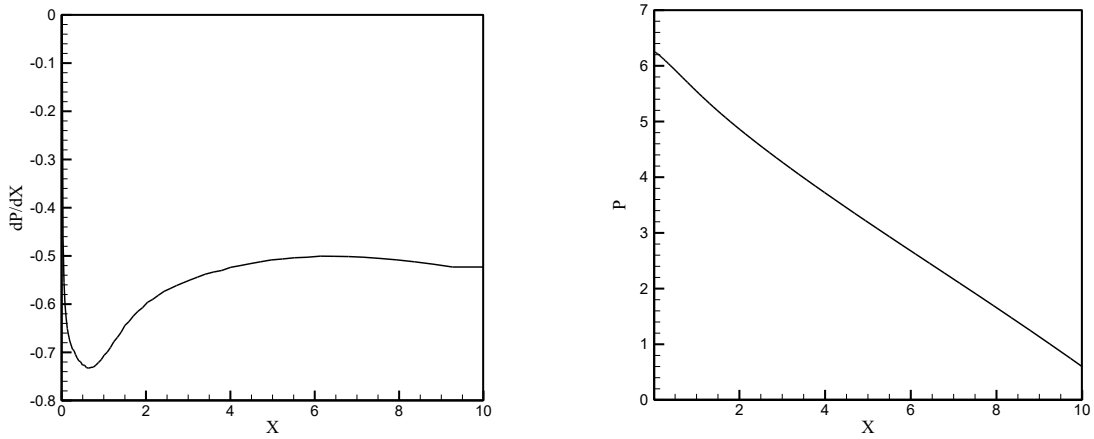


Fig. 8. Dimensionless pressure distribution and pressure drop along the channel centerline.

Fig. 9 illustrates the transverse temperature and nanoparticle concentration profiles at equidistant longitudinal stations. Thermal development follows Equation (19), characterized by boundary layer growth and increased bulk temperature due to surface heating. The profiles further confirm the symmetry boundary condition at the channel centerline. Regarding particle distribution, the initial injection is restricted to the upper half of the inlet, resulting in higher concentrations in that region near the entrance. However, nanoparticles gradually diffuse toward the centerline as the flow progresses. This migration is particularly evident near the exit, where particles accumulate centrally due to Brownian motion and thermophoresis driven by the increasing core temperature.

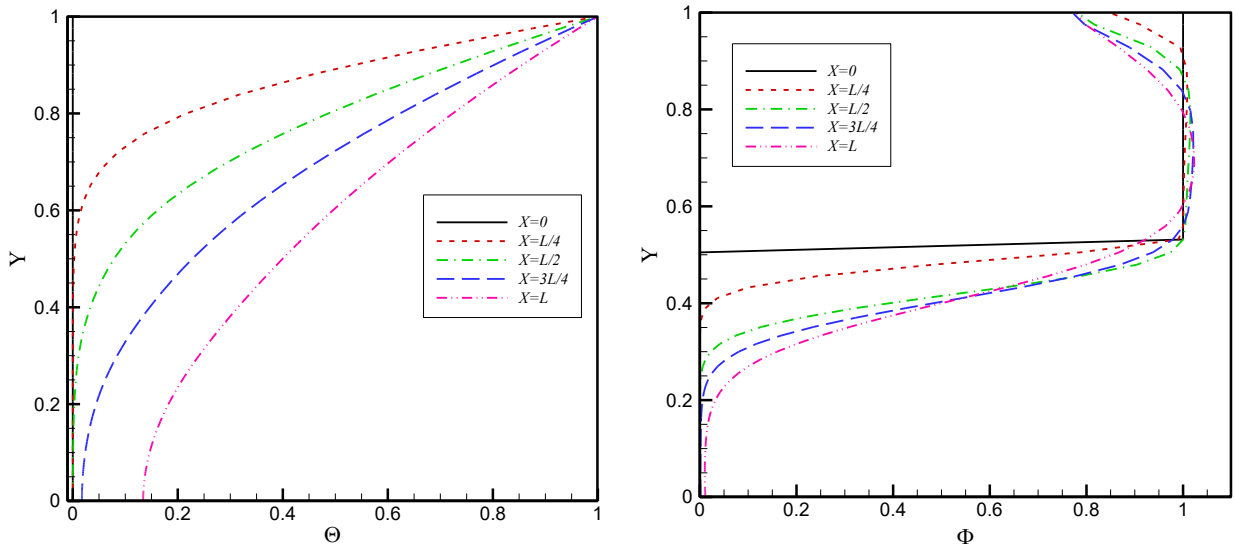


Fig. 9. Dimensionless temperature and nanoparticle concentration profiles at various axial locations along the channel.

Fig. 10 presents the axial distribution of the local Nusselt (Nu) and Sherwood (Sh) numbers along the channel wall. As expected, Nu decreases sharply in the entry region and stabilizes as it approaches the thermally fully developed state. This downstream reduction stems from the diminishing temperature gradient between the wall and the bulk fluid. Notably, the fully developed Nu significantly exceeds the values for a pure fluid, primarily due to the integrated effects of the porous medium and nanoparticle additives. Similarly, the local Sh declines along the channel, reflecting a reduced mass transfer rate as the nanoparticle distribution becomes more uniform downstream.

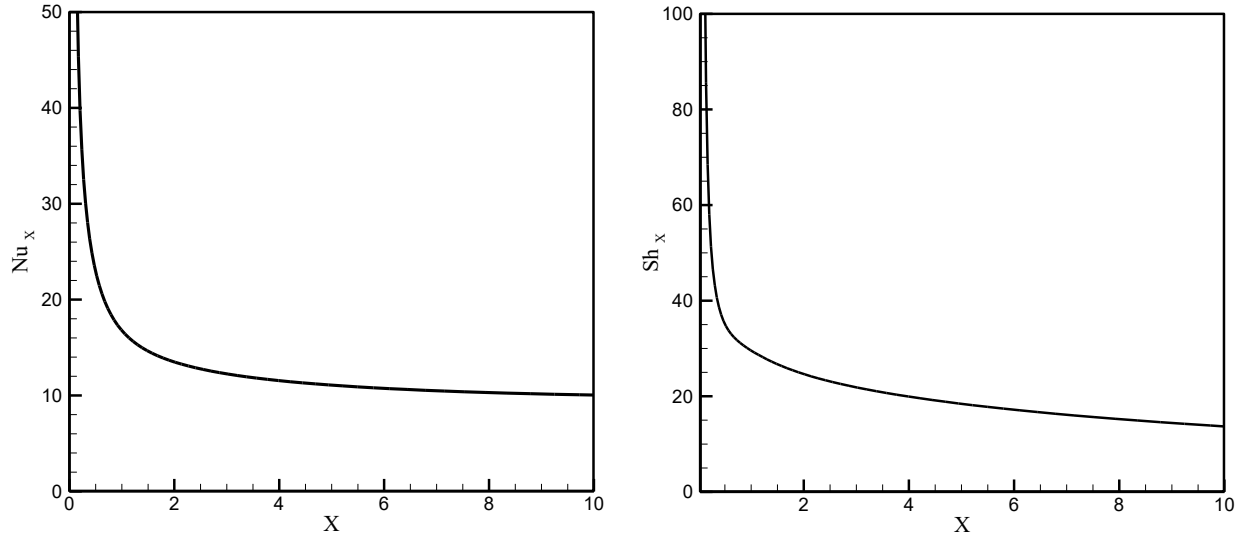


Fig. 10. Axial distribution of the local Nusselt and Sherwood numbers along the channel wall.

Following is the analysis of the influence of physical parameters on the hydrodynamic and thermal behavior of nanofluid flow in a porous-filled channel, encompassing pressure gradients, velocity, temperature and concentration distributions, as well as Nusselt and Sherwood numbers. While these flow characteristics are essential, the primary objective of this research is to investigate the thermal performance of the system. Consequently, the discussion primarily focuses on the effects of varying parameters on the temperature profiles and the Nusselt number.

The axial distribution of the dimensionless pressure gradient for various Reynolds number is shown in **Fig. 11**. As expected, increasing Re leads to a reduction in the dimensionless pressure drop across all sections, aligning with the decrease in the friction factor [87]. In the fully developed region, the pressure drop asymptotically stabilizes as the velocity profile becomes constant and kinetic energy changes cease. Notably, higher Re values delay the transition to fully developed conditions and extend the hydrodynamic entrance length. This is further reflected in the velocity profiles, where the peak velocity shifts towards the channel center upon reaching the developed state. Additionally, the maximum centerline velocity decreases at higher Re due to the reduced pressure gradient.

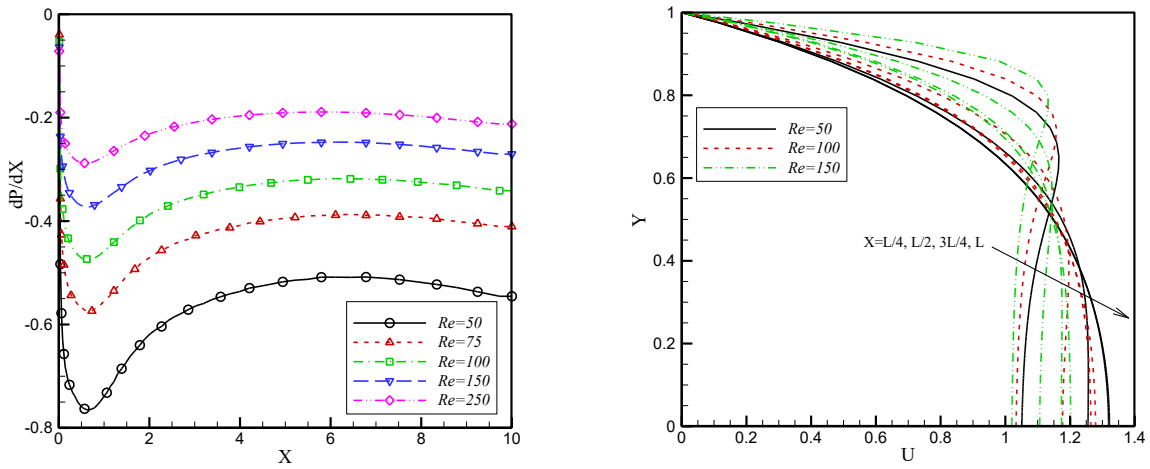


Fig. 11. Influence of Reynolds number on the dimensionless pressure drop and velocity profiles at various axial locations.

Fig. 12 illustrates the dimensionless temperature distribution for various Reynolds numbers within the laminar regime. As Re increases, the thermal penetration from the heated channel walls into the cold incoming fluid significantly decreases. Assuming constant fluid properties, a higher Re corresponds to an increased inlet velocity. Consequently, the fluid passes through the channel more rapidly, reducing the time for heat diffusion and shifting the temperature distribution toward the cold inlet conditions. This phenomenon is characterized by a noticeably thinner thermal boundary layer at higher Reynolds numbers.

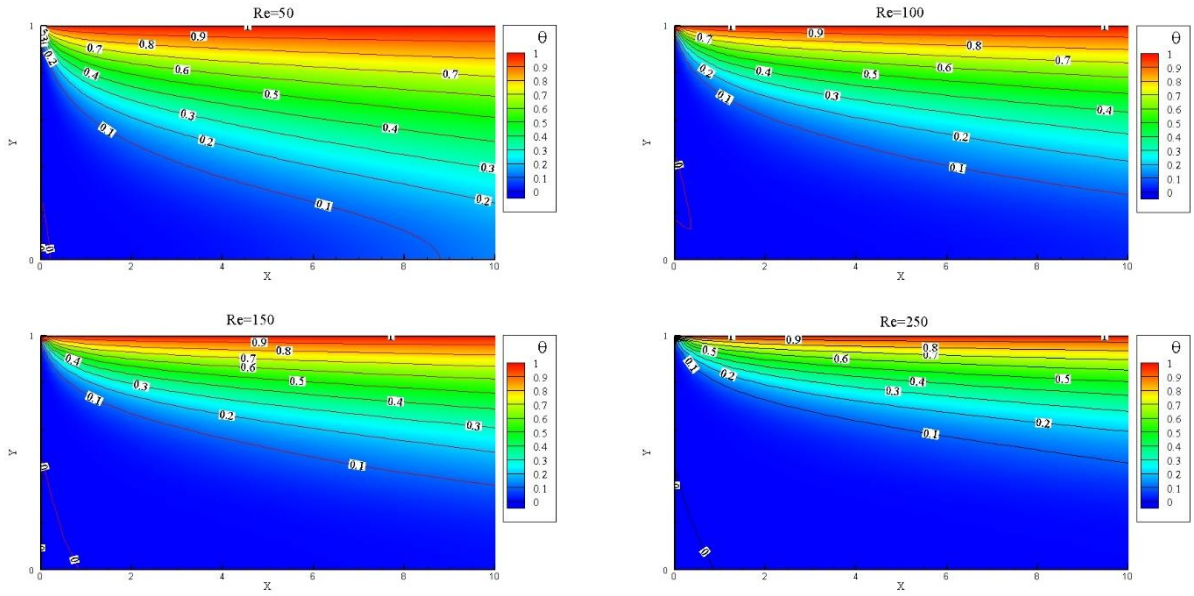


Fig. 12. Influence of Reynolds number on the dimensionless temperature contours of the nanofluid.

Fig. 13 displays the dimensionless concentration contours and the steady-state distribution of nanoparticles within the channel. As the Reynolds number increases, the nanoparticles' dispersion becomes significantly restricted, and their transport becomes more streamlined. This behavior is attributed to the dominance of inertial forces at higher Re, which diminishes the lateral diffusion of nanoparticles. Since the nanoparticles are injected into the boundary half of the channel, higher inertia further confines them to this region, causing their motion to align more closely with the primary flow direction.

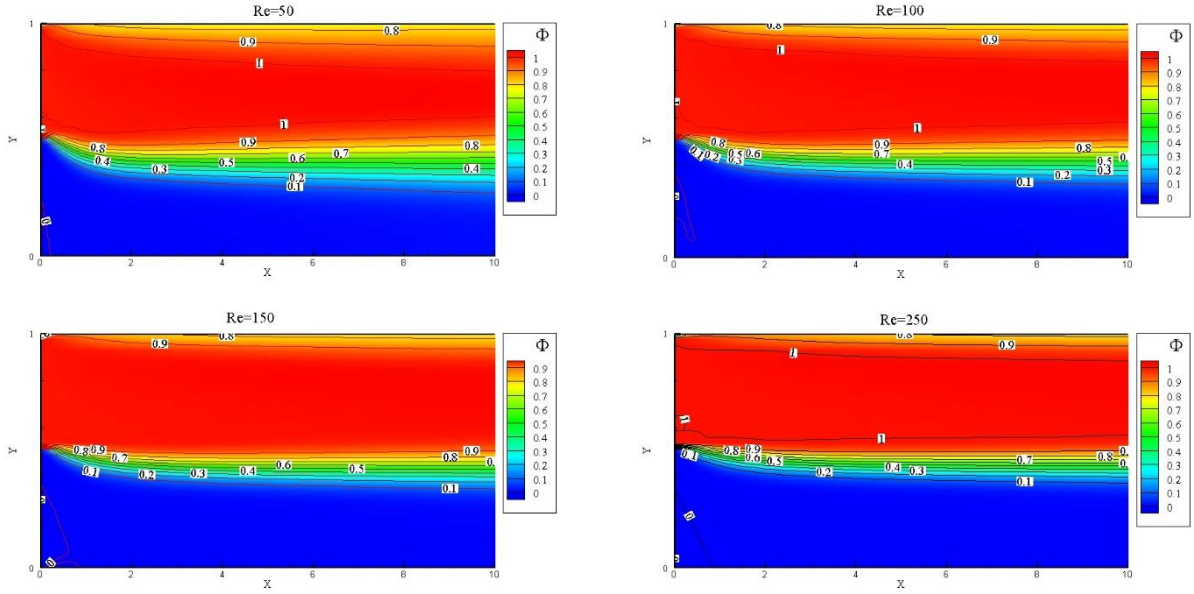


Fig. 13. Influence of Reynolds number on the dimensionless nanoparticle concentration contours.

Fig. 14 shows that increasing Re significantly enhances the local Nusselt number. This is attributed to higher fluid velocities and steeper wall temperature gradients (as seen in Fig. 12), which increase the convective heat transfer coefficient. Similarly, this Figure illustrates a sharp rise in the Sherwood number with Re, driven by intensified convective mass transport. Furthermore, higher Reynolds numbers extend both the thermal and concentration entrance lengths, delaying the onset of fully developed conditions. The transition to a fully developed state is indicated by the curves asymptotically reaching a horizontal constant value.

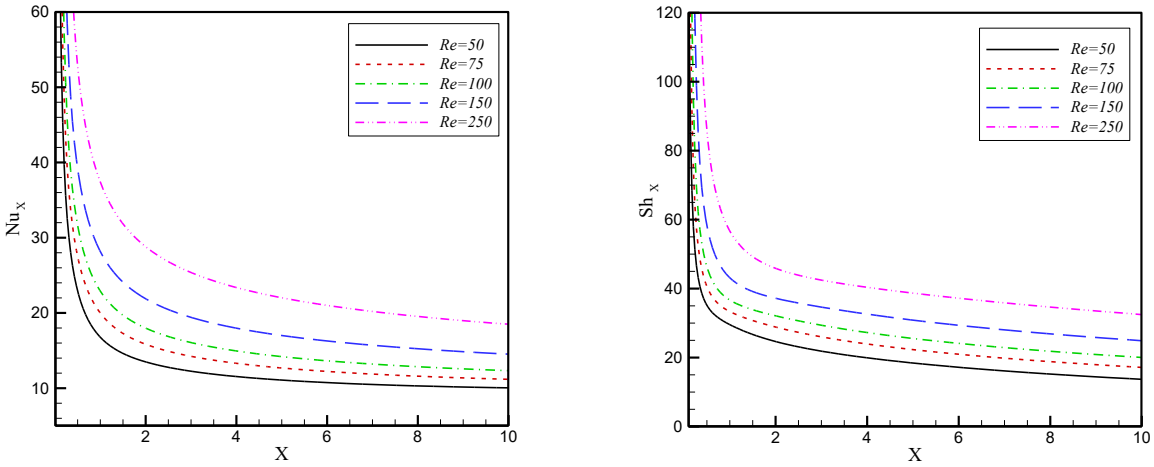


Fig. 14. Influence of Reynolds number on the local Nusselt and Sherwood numbers along the channel walls.

One of the most significant findings of this study is presented in **Fig. 15**, which shows a substantial increase in the local Nusselt number as the inlet nanoparticle concentration rises. This enhancement is primarily driven by the increased thermal conductivity of the nanofluid, which steepens the temperature gradient at the channel walls. Similarly, the Sherwood number exhibits a marked increase, particularly in the fully developed region, indicating enhanced convective mass transport at higher concentrations. Quantitative data in **Table 4** further supports these observations. The injection of only a 1% volume fraction of nanoparticles results in an 8.28% increase in the average Nusselt number, while increasing the concentration to 8% leads to a remarkable enhancement of over 56% compared to the base fluid.

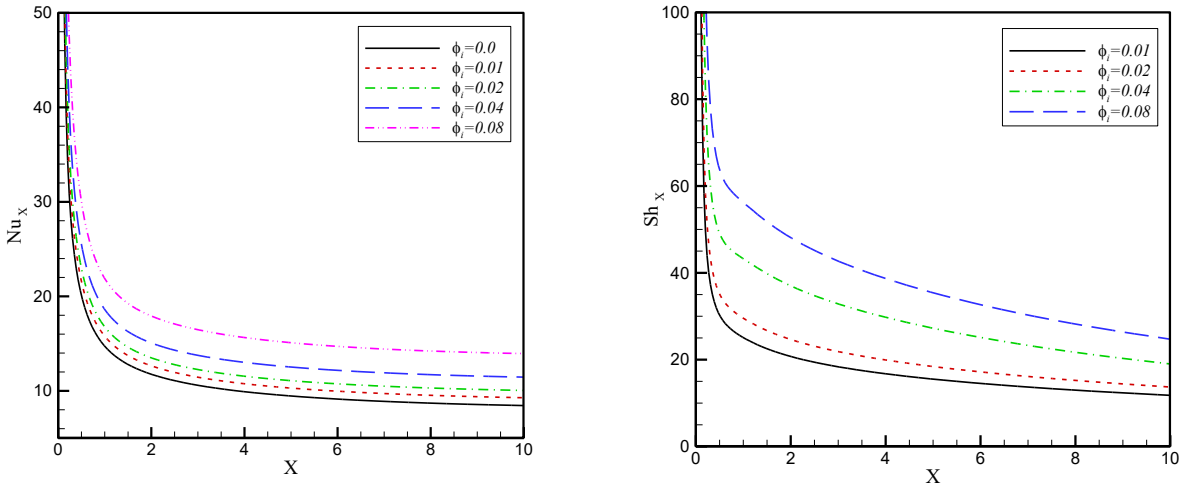


Fig. 15. Influence of inlet nanoparticle volume fraction on the local Nusselt and Sherwood numbers.

Table 4. Average Nusselt numbers and corresponding enhancements relative to the base fluid for varying nanoparticle concentrations.

Fluid Type	**Inlet Nanoparticle Concentration (ϕ_i)**	**Average Nusselt Number ($\overline{Nu}$)**	**Enhancement** $(\frac{\overline{Nu}_{nf} - \overline{Nu}_f}{\overline{Nu}_f}) \times 100$
Pure Water	$\phi_i = 0.0$	11.52553	-
Cu-Water Nanofluid	$\phi_i = 0.01$	12.47937	8.28%
Cu-Water Nanofluid	$\phi_i = 0.02$	13.37597	16.05%
Cu-Water Nanofluid	$\phi_i = 0.04$	15.03284	30.43%
Cu-Water Nanofluid	$\phi_i = 0.08$	18.00932	56.25%

Fig. 16 reveals that while nanoparticle injection significantly enhances thermal development, the system becomes remarkably insensitive to the injection thickness beyond $S = 0$. This suggests that thermal boundary layer modification is effectively optimized by localized near-wall particle concentrations. Driven by Brownian motion and thermophoresis, these particles bolster thermal diffusivity in high-gradient regions, rendering further volumetric coverage redundant. Notably, the boundary distribution induces a particularly sharp temperature gradient at the channel wall due to the strategic presence of nanoparticles within the inner boundary layer. This localized intensification indicates that substantial convective gains are attainable at minimal injection depths, a trend to be definitively quantified through the subsequent analysis of Nusselt number profiles.

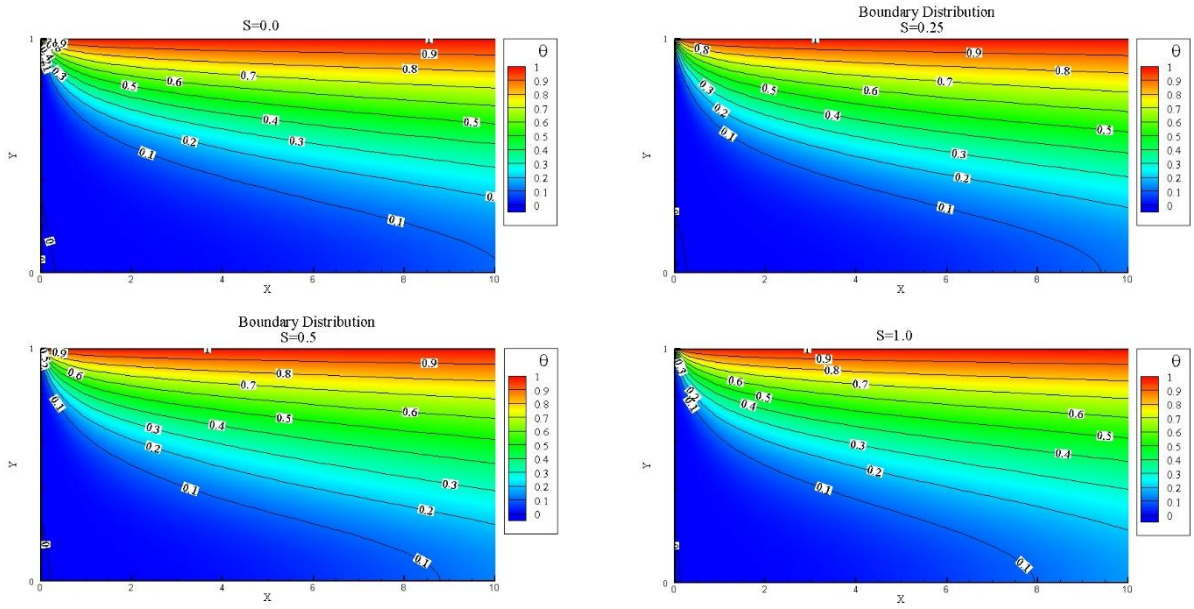
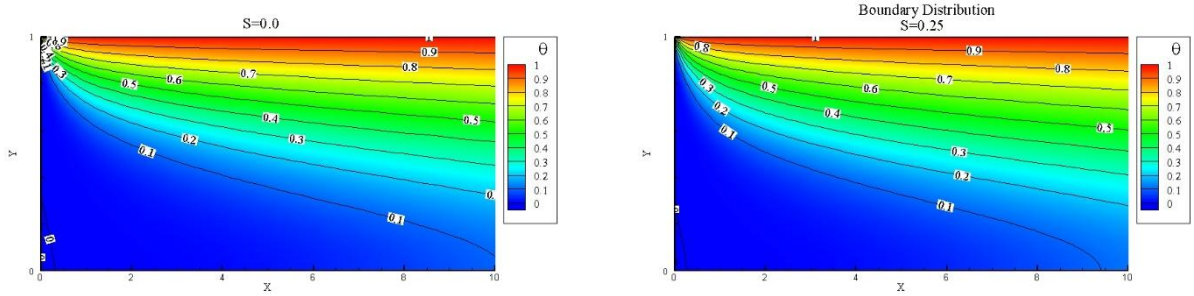


Fig. 16. Effect of the dimensionless inlet injection thickness on the dimensionless temperature contours of the nanofluid.

The dimensionless concentration (ϕ) contours in **Fig. 17** elucidate the physical mechanisms underlying the observed thermal saturation. At $S = 0.25$, boundary injection establishes a dense nanoparticle layer ($\phi = 1.0$) within the critical near-wall region, effectively targeting the zone of maximum thermal resistance. While increasing the injection depth to $S = 1.0$ eventually permeates the entire channel core, the near-wall concentration remains remarkably consistent. This confirms that convective enhancement is predominantly driven by localized boundary layer modification, rendering further volumetric coverage in the bulk flow redundant for energy dissipation.



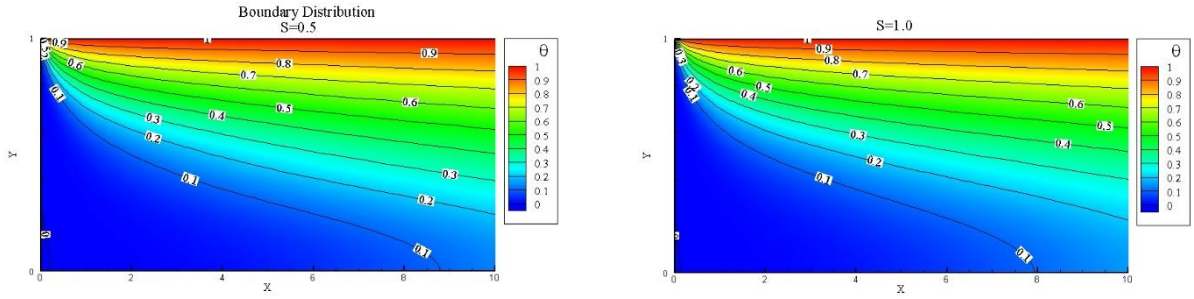


Fig. 17. Effect of the dimensionless inlet injection thickness on the dimensionless temperature contours of the nanofluid.

The longitudinal evolution of the local Nusselt (Nu_X) and Sherwood (Sh_X) numbers along the channel wall for various dimensionless injection thicknesses is illustrated in **Fig. 18**. While nanoparticle injection clearly enhances convective heat transfer, the thermal response exhibits a remarkable insensitivity to the total injection width. Due to Brownian diffusion, localized near-wall injection achieves thermal performance comparable to full-channel loading by effectively targeting the high-gradient boundary layer. As the flow progresses downstream, the Nu_X profiles for all injection thicknesses converge, indicating that spatial dispersion becomes uniform in the fully developed region. Similarly, the local Sherwood number converges to a consistent value for higher injection thicknesses, suggesting that mass transport near the wall becomes independent of the initial layer width in regions far from the inlet. However, distinct variations in mass transfer rates remain evident near the entrance, where the initial concentration gradients are most pronounced.

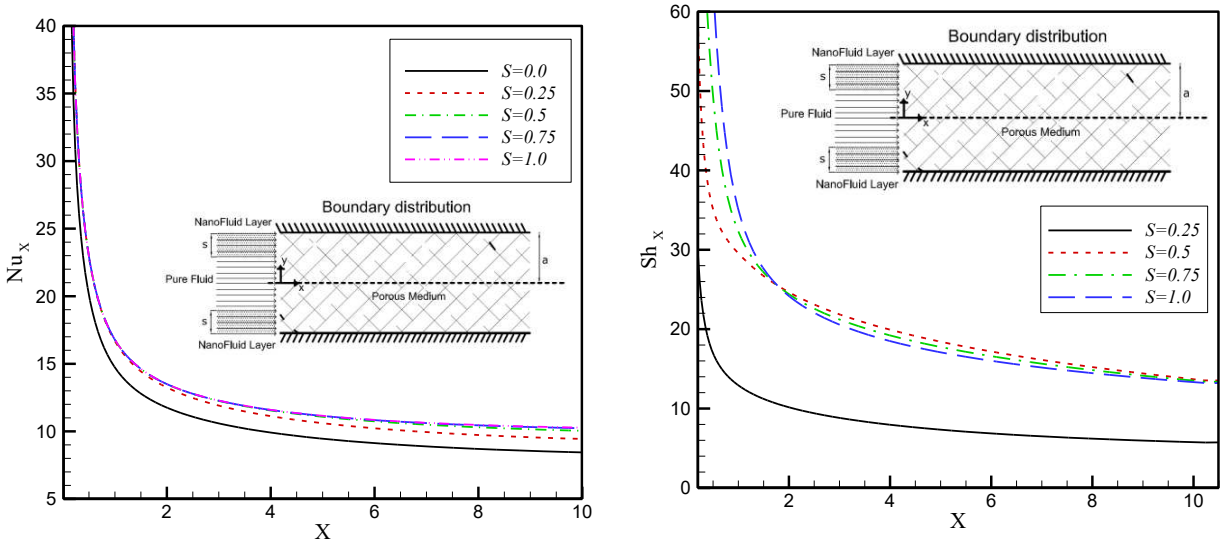


Fig. 18. Effect of the dimensionless inlet injection thickness with boundary distribution on the local Nusselt number (left) and the local Sherwood number (right) along the channel wall.

Table 5 presents the average Nusselt number $(\overline{Nu})$ along the channel wall and its percentage enhancement relative to the base fluid for various nanoparticle injection thicknesses. The data highlights a critical economic finding: full-channel injection $(S = 1.0)$ increases the average Nusselt number by less than 1% compared to a 50% boundary injection $(S = 0.5)$. Furthermore, expanding the injection from $(S = 0.75)$ to a full distribution results in a negligible gain of only 0.2%. These results underscore that localized boundary injection is highly cost effective because it offers near maximal thermal performance while requiring significantly lower nanoparticle consumption.

Table 5. Average Nusselt number and percentage enhancement for different injection thicknesses (Boundary Distribution)

Case	Injection Thickness (S)	Average Nusselt $(\overline{Nu})$	Enhancement $(\frac{\overline{Nu}_{nf} - \overline{Nu}_f}{\overline{Nu}_f}) \times 100$
Pure Water	0.0	11.52553	-
Water + Cu Nanofluid	0.25	12.94951	12.35%
Water + Cu Nanofluid	0.5	13.37597	16.05%
Water + Cu Nanofluid	0.75	13.45672	16.76%
Water + Cu Nanofluid	1.0	13.47749	16.94%

Fig. 19 represents one of the most significant cornerstones of this research. It illustrates the substantial increase in the local Nusselt number (Nu_X) resulting from the enhancement of the thermal dispersion coefficient (C^*). Physically, an increase in the dispersion coefficient bolsters the effective thermal conductivity of the nanofluid, thereby facilitating greater heat transfer from the channel wall and driving the growth of the Nusselt number. Given this profound impact, manipulating thermal dispersion emerges as one of the simplest and most cost-effective strategies for intensifying heat transfer. Additionally, this figure reveals a simultaneous rise in the local Sherwood number (Sh_X) as the dispersion coefficient increases, signifying enhanced nanoparticle mass transport through convective mechanisms.

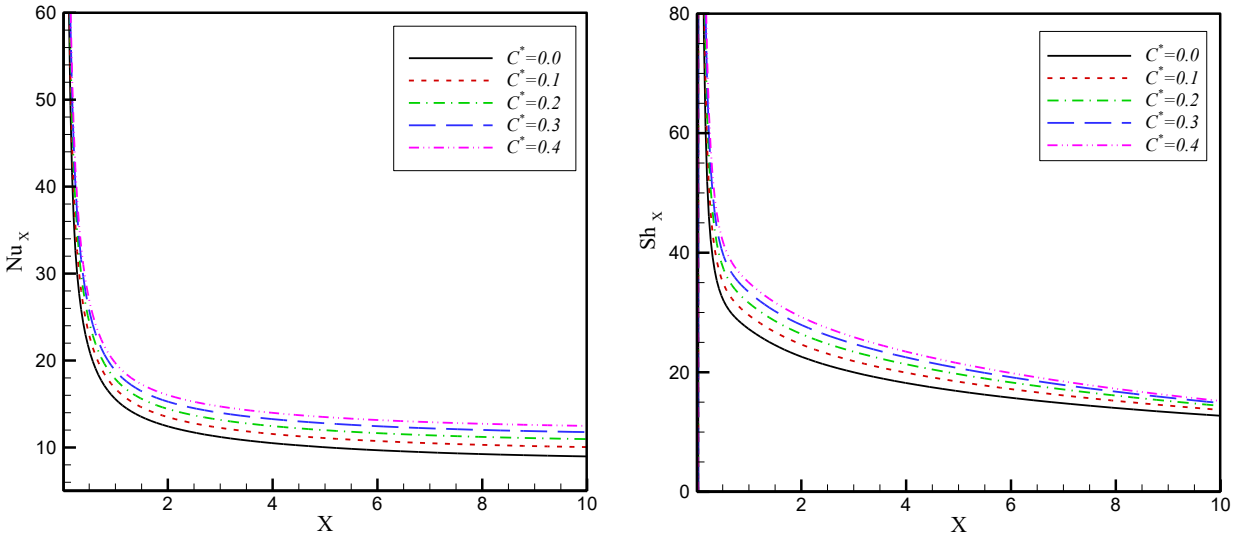


Fig. 19. Effect of the thermal dispersion coefficient on the local Nusselt number (left) and the local Sherwood number (right) along the channel wall.

The integration of nanoparticles into the base fluid fundamentally alters the hydrothermal characteristics of the flow field, as evidenced by the substantial enhancement in thermal profiles and convective heat transfer rates compared to pure water. As depicted in the local Nusselt number distributions in **Fig. 20**, the transition from a pure fluid to a nanofluid significantly augments the flow field temperature, thereby facilitating more efficient heating from the channel walls. While the specific material of the nanoparticles exerts a relatively subtle influence on the Nu_X curves, **Table 6** reveals that even a marginal volume fraction of 2% yields a remarkable increase in the average Nusselt number, reaching a peak enhancement of 16.05% for the Cu-Water nanofluid suspension. Conversely, the mass transfer analysis illustrated in the Sh_X profiles indicates a distinct trend where the chemical nature of the additives becomes more decisive; the superior dispersion of titania particles leads to a significantly higher Sherwood number compared to other investigated variants. This suggests that while metallic copper is optimal for thermal intensification due to its higher conductivity, TiO_2 provides more pronounced concentration gradients, effectively maximizing the mass transport efficiency within the channel.

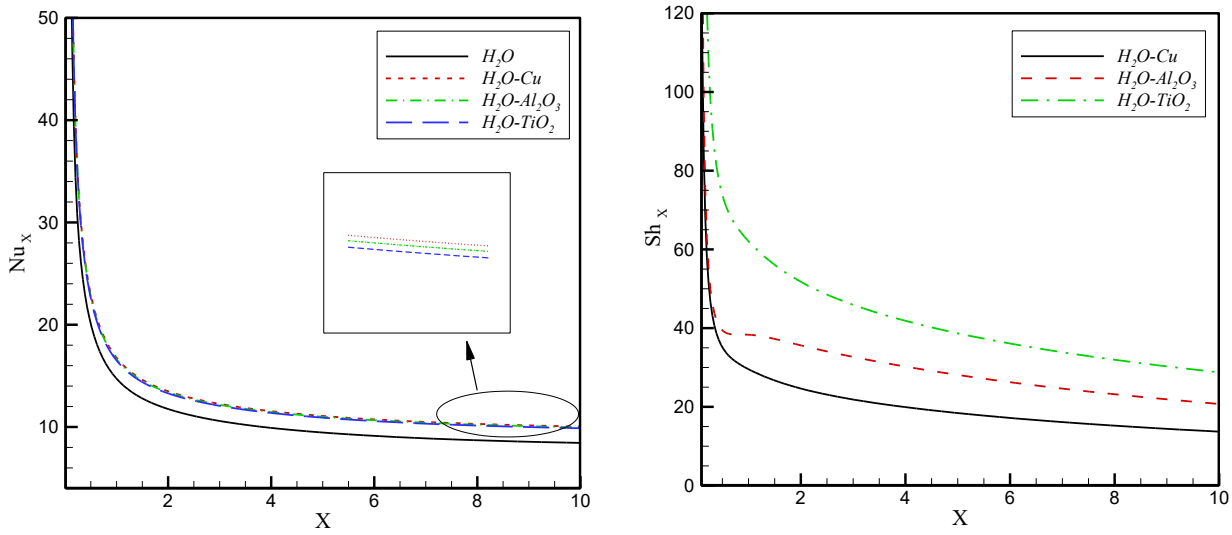


Fig. 20. Effect of nanoparticle type on the local Nusselt number (left) and Sherwood number (right) along the channel wall.

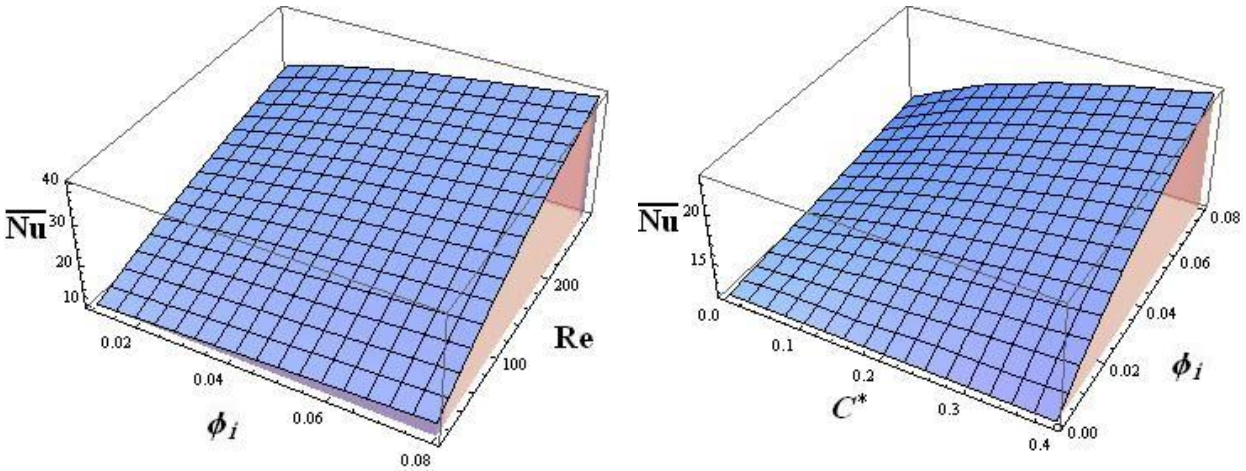
Table 6 Average Nusselt number and percentage enhancement for nanoparticle type

Nanofluid Type	Average Wall Nusselt Number $(\overline{Nu})$	Enhancement $(\frac{\overline{Nu}_{nf} - \overline{Nu}_f}{\overline{Nu}_f}) \times 100$
H_2O	11.52553	-
H_2O/Cu	13.37579	16.05%
H_2O/Al_2O_3	13.26931	15.13%
H_2O/TiO_2	13.15559	14.14%

The thermal analysis thus far has focused on the local Nusselt number (Nu_X) along the channel. However, to evaluate the system's overall thermal performance, the average Nusselt number $(\overline{Nu})$ must be calculated according to Equation (26). As the primary metric for the convective heat transfer coefficient, $\overline{Nu}$ provides a definitive measure of the total heat exchanged between the constant-temperature wall and the flowing nanofluid. This section investigates how the governing physical parameters influence this average value. **Fig. 21** presents 3D surface plots illustrating the coupled effects of the Reynolds number (Re), inlet nanoparticle volume fraction (ϕ_i), thermal dispersion

coefficient (C^*), dimensionless inlet injection thickness (S), and nanoparticle diameter (d_P) on the average Nusselt number $(\overline{Nu})$ of the channel wall.

- **Reynolds Number and Concentration:** As shown in the top-left plot, $\overline{Nu}$ increases significantly with flow inertia (Re) and nanoparticle concentration (ϕ_i). A synergistic effect is observed where higher Re intensifies the sensitivity of heat transfer to ϕ_i.
- **Thermal Dispersion and Concentration:** The interaction between the dispersion coefficient (C^*) and volume fraction is depicted in the top-right plot. The role of C^* becomes increasingly dominant at higher volume fractions, where its enhancement leads to a sharp escalation in average thermal performance.
- **Injection Thickness and Concentration:** The bottom-left plot illustrates that enhancing the injection width up to $S \approx 0.5$ results in a steep rise in $\overline{Nu}$. Beyond this point, further expansion yields diminishing returns with negligible impact on overall heat transfer.
- **Nanoparticle Diameter and Concentration:** The bottom-right plot highlights that utilizing smaller nanoparticles (d_P) improves thermal conditions. This advantage is most pronounced at elevated volume fractions.



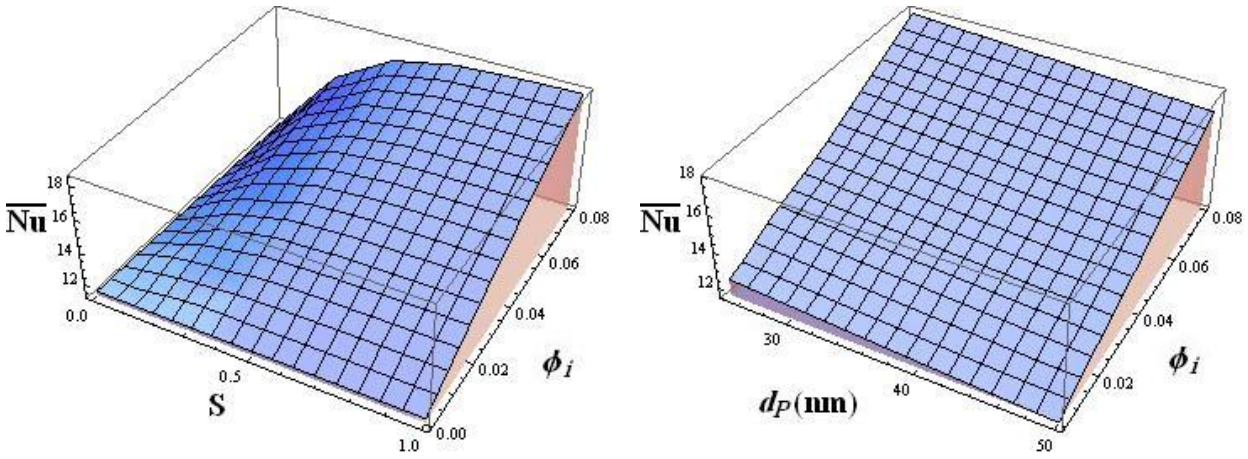


Fig. 21. 3D profiles of the average Nusselt number versus governing physical parameters.

6. Conclusions

This study presents a precise numerical investigation of the hydrothermal behavior of nanofluids within a Darcy-Forchheimer porous channel using the Buongiorno two-phase model. By solving the complete system of non-linear governing PDEs via a Fortran-based SIMPLER algorithm, the complex interplay between thermal dispersion, slip mechanisms, and partial nanoparticle injection was elucidated. The key findings of this research are summarized as follows:

I. **Nanoparticle Material Comparison:** Among the three investigated nanoparticles *(Cu*, Al_2O_3 *and* TiO_2*)*, the Cu-water nanofluid demonstrates the most significant heat transfer enhancement. Due to its superior thermal conductivity ($400\ W/m.K$), it achieves the highest average Nusselt number.

II. **Strategic Partial Injection:** A critical economic and thermal finding is that full-channel injection is not necessary. The results indicate that a 50% boundary injection provides nearly the same thermal performance as 100% saturation, with the difference in Nusselt number being less than 1%. This proves that localized injection is highly cost-effective by

reducing nanoparticle consumption significantly while maintaining maximal cooling efficiency.

III. **Thermal Dispersion Effect:** Elevating the thermal dispersion coefficient notably enhances lateral heat transport, which in turn intensifies the convective heat transfer rate across the porous matrix.

IV. **Influence of Concentration:** Increasing the inlet volume fraction from 0% to 2% for Cu-water nanofluid leads to a peak enhancement of 16.05% in the average Nusselt number, highlighting the strong role of nanoparticle concentration in boosting thermal performance.

V. **Asymptotic Behavior:** The system exhibits an asymptotic response to the injection thickness. Beyond a dimensionless thickness of $S = 0.5$, further expansion of the nanoparticle zone yields negligible improvements in the heat transfer rate.

Funding

The authors declare that no funds, grants, or other support were received during the preparation of this manuscript.

REFERENCES

[1] S.U.S. Choi, J.A. Eastman, ENHANCING THERMAL CONDUCTIVITY OF FLUIDS WITH NANOPARTICLES, (n.d.).

[2] J.A. Eastman, U.S. Choi, S. Li, L.J. Thompson, S. Lee, Enhanced Thermal Conductivity through the Development of Nanofluids, MRS Online Proc. Libr. 457 (1996) 3–11. https://doi.org/10.1557/PROC-457-3.

[3] J. Buongiorno, Convective Transport in Nanofluids, J. Heat Transf. 128 (2006) 240–250. https://doi.org/10.1115/1.2150834.

[4] R.K. Tiwari, M.K. Das, Heat transfer augmentation in a two-sided lid-driven differentially heated square cavity utilizing nanofluids, Int. J. Heat Mass Transf. 50 (2007) 2002–2018. https://doi.org/10.1016/j.ijheatmasstransfer.2006.09.034.

[5] S. Abelman, A. Basiri Parsa, H.O. Sayehvand, Nanofluid flow and heat transfer in a Brinkman porous channel with variable porosity: Quaestiones Mathematicae: Vol 41, No 4, (n.d.). https://www.tandfonline.com/doi/abs/10.2989/16073606.2017.1404503 (accessed December 13, 2025).

[6] Muhammad, M. Sarfraz, M. Khan, A.S. Alqahtani, M.Y. Malik, Simulation of gyrotactic microorganisms in Jeffrey nanofluid using Buongiorno model and Ohmic heating, Alex. Eng. J. 100 (2024) 32–41. https://doi.org/10.1016/j.aej.2024.05.010.

[7] H.-O. Sayehvand, A. Basiri Parsa, A new numerical method for investigation of thermophoresis and Brownian motion effects on MHD nanofluid flow and heat transfer between parallel plates partially filled with a porous medium, Results Phys. 7 (2017) 1595–1607. https://doi.org/10.1016/j.rinp.2017.02.004.

[8] C. Fetecau, D. Vieru, W.A. Azhar, C. Fetecau, D. Vieru, W.A. Azhar, Natural Convection Flow of Fractional Nanofluids Over an Isothermal Vertical Plate with Thermal Radiation, Appl. Sci. 7 (2017). https://doi.org/10.3390/app7030247.

[9] M.M. Bhatti, M.M. Rashidi, Effects of thermo-diffusion and thermal radiation on Williamson nanofluid over a porous shrinking/stretching sheet, J. Mol. Liq. 221 (2016) 567–573. https://doi.org/10.1016/j.molliq.2016.05.049.

[10] A.-R.A. Khaled, K. Vafai, Heat transfer enhancement through control of thermal dispersion effects, Int. J. Heat Mass Transf. 48 (2005) 2172–2185. https://doi.org/10.1016/j.ijheatmasstransfer.2004.12.035.

[11] S.M. Mousavi, S. Khasi, S.L. Bryant, A. Kantzas, Surface engineered Nanofluids in geothermal systems: Experimental evaluation of enhancement in chemical and thermal stability of Nanofluids and numerical investigation of the effect of nanoparticles in heat transfer and pressure drop characteristics, J. Mol. Liq. 434 (2025) 128030. https://doi.org/10.1016/j.molliq.2025.128030.

[12] G. He, Z. Luo, C. Li, S. Qing, J. Zhang, X. Zhang, Molecular dynamics investigation of interfacial thermal transport for enhanced heat transfer in Al–Cu/H2O hybrid Nanofluids, Chem. Phys. 602 (2026) 113006. https://doi.org/10.1016/j.chemphys.2025.113006.

[13] A. Khan, Hashim, M. Farooq, S.M. Hussain, H. Ahmad, W. Jamshed, M.R. Eid, N. Sirelkhtam Elmki Abdalla, Heat and mass transfer in magnetic Casson nanofluids flow with radiation and stratification effects: Thermal management applications, J. Radiat. Res. Appl. Sci. 18 (2025) 102019. https://doi.org/10.1016/j.jrras.2025.102019.

[14] Q.-H. Shi, A. Hamid, M.I. Khan, R.N. Kumar, R.J.P. Gowda, B.C. Prasannakumara, N.A. Shah, S.U. Khan, J.D. Chung, Numerical study of bio-convection flow of magneto-cross nanofluid containing gyrotactic microorganisms with activation energy, Sci. Rep. 11 (2021) 16030. https://doi.org/10.1038/s41598-021-95587-2.

[15] T. Hayat, I. Ullah, K. Muhammad, A. Alsaedi, Finite difference analysis of power-law nanofluid with thermal radiation and bioconvection, Int. J. Mod. Phys. B 38 (2024) 2450008. https://doi.org/10.1142/S0217979224500085.

[16] Y.-M. Chu, M.I. Khan, N.B. Khan, S. Kadry, S.U. Khan, I. Tlili, M.K. Nayak, Significance of activation energy, bio-convection and magnetohydrodynamic in flow of third grade fluid (non-Newtonian) towards stretched surface: A Buongiorno model analysis, Int. Commun. Heat Mass Transf. 118 (2020) 104893. https://doi.org/10.1016/j.icheatmasstransfer.2020.104893.

[17] M. Qasim, Z.H. Khan, R.J. Lopez, W.A. Khan, Heat and mass transfer in nanofluid thin film over an unsteady stretching sheet using Buongiorno's model, Eur. Phys. J. Plus 131 (2016) 16. https://doi.org/10.1140/epjp/i2016-16016-8.

[18] S. Nadeem, W. Fuzhang, F.M. Alharbi, F. Sajid, N. Abbas, A.S. El-Shafay, F.S. Al-Mubaddel, Numerical computations for Buongiorno nano fluid model on the boundary layer flow of viscoelastic fluid towards a nonlinear stretching sheet, Alex. Eng. J. 61 (2022) 1769–1778. https://doi.org/10.1016/j.aej.2021.11.013.

[19] N.C. Roşca, A.V. Roşca, E.H. Aly, I. Pop, Flow and heat transfer past a stretching/shrinking sheet using modified Buongiorno nanoliquid model, Mathematics 9 (2021) 3047.

[20] Adnan, A. Rasheed, D.L.C. Ching, A. Eladeb, L. Kolsi, W. Rajhi, I. Khan, I. Tlili, Investigation of unsteady Buongiorno nanofluid in a slanted thermally radiated revolving channel under upstream microbial movement in the

absence of chemical reaction, J. Radiat. Res. Appl. Sci. 17 (2024) 101120. https://doi.org/10.1016/j.jrras.2024.101120.
[21] M.A.Z. Raja, A. Latif, M. Shamim, K.S. Nisar, M. Shoaib, Design of artificial neural network for buongiorno model with nanofluids flow through stretching sheet, Case Stud. Therm. Eng. 69 (2025) 106054. https://doi.org/10.1016/j.csite.2025.106054.
[22] K.M. Nihaal, U.S. Mahabaleshwar, Heat and mass transfer analysis of hybrid nanofluid flow over a rotating permeable cylinder: A modified Buongiorno model approach, Hybrid Adv. 6 (2024) 100243. https://doi.org/10.1016/j.hybadv.2024.100243.
[23] Adnan, K.U. Rahman, Z. Mahmood, S.U. Khan, A. Ali, Z. Li, I. Tlili, Enhanced thermal study in hybrid nanofluid flow in a channel motivated by graphene/Fe3O4 and Newtonian heating, Results Eng. 21 (2024) 101772. https://doi.org/10.1016/j.rineng.2024.101772.
[24] S.S.U. Devi, S.P.A. Devi, Numerical investigation of three-dimensional hybrid Cu–Al2O3/water nanofluid flow over a stretching sheet with effecting Lorentz force subject to Newtonian heating, Can. J. Phys. 94 (2016) 490–496. https://doi.org/10.1139/cjp-2015-0799.
[25] P. Rana, R. Dhanai, L. Kumar, MHD slip flow and heat transfer of Al2O3-water nanofluid over a horizontal shrinking cylinder using Buongiorno's model: Effect of nanolayer and nanoparticle diameter, Adv. Powder Technol. 28 (2017) 1727–1738. https://doi.org/10.1016/j.apt.2017.04.010.
[26] S. Ramadevu, P.V. Kumar, G. Lorenzini, S.M. Ibrahim, K. Jyothsna, Viscoelastic Flow Analysis with Buongiorno Nanofluid Model over a Nonlinear Stretching Sheet: A Homotopy Approach, Front. Heat Mass Transf. 23 (2025) 857–879. https://doi.org/10.32604/fhmt.2025.062231.
[27] M.M. Nandeppanavar, H. Basha, S. Udgiri, Analysis of bio-convective gyrotactic microorganisms swim in a Buongiorno's dissipative Prandtl-Eyring nanofluid flow about a stretching sheet with inclined magnetic field and radiation effects under chemical reaction, Hybrid Adv. 8 (2025) 100382. https://doi.org/10.1016/j.hybadv.2025.100382.
[28] J. Raza, S. Dero, L.A. Lund, Z. Omar, Duality and stability of MHD Darcy–Forchheimer porous medium flow of rotating nanofluid on a linear shrinking/stretching sheet: Buongiorno model, Int. J. Numer. Methods Heat Fluid Flow 32 (2022) 1517–1539.
[29] N.C. Roşca, A.V. Roşca, E.H. Aly, I. Pop, Semi-analytical solution for the flow of a nanofluid over a permeable stretching/shrinking sheet with velocity slip using Buongiorno's mathematical model, Eur. J. Mech. - BFluids 58 (2016) 39–49. https://doi.org/10.1016/j.euromechflu.2016.01.008.
[30] P. Asaigeethan, K. Vaithiyalingam, K. Loganathan, Computational study of Carreau nanofluid across a stretching cylinder by homogeneous-heterogeneous responses: A frame work of modified Buongiorno's nanofluid model, Partial Differ. Equ. Appl. Math. 11 (2024) 100780. https://doi.org/10.1016/j.padiff.2024.100780.
[31] P. Asaigeethan, K. Vaithiyalingam, K. Loganathan, K. Prabu, M. Abbas, N.K. Mishra, Numerical study of Carreau fuzzy nanofluid across a stretching cylinder using a modified version of Buongiorno's nanofluid model, Alex. Eng. J. 101 (2024) 318–329. https://doi.org/10.1016/j.aej.2024.05.095.
[32] R.P. Ashrith, K.V. Nagaraja, P. Nimmy, P. Patel, A. Kulshreshta, J.K. Madhukesh, C. Prakash, Endothermic and exothermic reactions and stagnation point nanofluid flow over a porous stretched surface with a revised Buongiorno model, South Afr. J. Chem. Eng. 52 (2025) 141–150. https://doi.org/10.1016/j.sajce.2025.02.003.
[33] S. Manjunatha, R. Manaswini, P.M. Ioan, T.N. Tanuja, Flow and heat transfer of penta-hybrid nanofluid at stagnation point over a stretching/shrinking sheet, Therm. Sci. Eng. Prog. 64 (2025) 103797. https://doi.org/10.1016/j.tsep.2025.103797.
[34] F. Nazir, J. Ahmed, T. Abdeljawad, A. Alshamrani, K.M. Abualnaja, M.A. Elkotb, Analysis of thermal and solutal transport in Casson nanofluid flow around a rotating cylinder subject to mixed convection and radiation, Case Stud. Therm. Eng. 74 (2025) 106663. https://doi.org/10.1016/j.csite.2025.106663.
[35] M. Bhatti, R. Ellahi, S. Sait, Numerical investigation of magnetized nanofluid flow in a non-Darcian medium with convective heating conditions across a rotating disk, Int. J. Numer. Methods Heat Fluid Flow (2025). https://www.semanticscholar.org/paper/Numerical-investigation-of-magnetized-nanofluid-in-Bhatti-Ellahi/62f2e8a9ddad4ea162afe11189aca0b3363c89f7 (accessed December 13, 2025).
[36] I.J. Supti, Md.Z. Hossain, Md.M. Molla, Magnetohydrodynamic double diffusive mixed convection of power-law non-Newtonian hybrid nanofluid in rotating eccentric annuli with different positions of inner cylinder, South Afr. J. Chem. Eng. 54 (2025) 546–566. https://doi.org/10.1016/j.sajce.2025.09.011.
[37] T. Anwar, Q. Raza, T. Mushtaq, B. Ali, E. Hemati, MHD Casson Nanofluid Flow over a Stretching Rotating Disk with Heat Source and Spatially Varying Magnetic Field, Int. J. Thermofluids 30 (2025) 101422. https://doi.org/10.1016/j.ijft.2025.101422.
[38] R.D. Alsemiry, S.A. Hussein, A.A.M. Arafa, M. Abdel-Haleem, K. Lotfy, M.R. Eid, E.M. Elsaid, Metachronal flagellar waves analysis in hydromagnetic Oldroyd-4 nanofluid flow: Thermal radiative peristaltic motion via

symmetric channel with flagellated walls, J. Radiat. Res. Appl. Sci. 18 (2025) 101477. https://doi.org/10.1016/j.jrras.2025.101477.
[39] E.O. Fatunmbi, O.L. Aako, Hydromagnetic micropolar nanofluid heat and mass transfer in a porous channel with thermophoresis, brownian motion and non-uniform heat source, Nano-Struct. Nano-Objects 41 (2025) 101456. https://doi.org/10.1016/j.nanoso.2025.101456.
[40] M.A. Basit, M. Imran, R. Safdar, M. Tahir, M.R. Ali, A.S. Hendy, A. Alhushaybari, A.M. Alharthi, Thermally radiative bioconvective nanofluid flow on a wavy cylinder with buongiorno model: A sensitivity analysis using response surface methodology, Case Stud. Therm. Eng. 55 (2024) 104178. https://doi.org/10.1016/j.csite.2024.104178.
[41] M. Turkyilmazoglu, Buongiorno model in a nanofluid filled asymmetric channel fulfilling zero net particle flux at the walls, Int. J. Heat Mass Transf. 126 (2018) 974–979. https://doi.org/10.1016/j.ijheatmasstransfer.2018.05.093.
[42] W. Ahmad, S. Rehman, U. Riaz, M. Saqib, Jeffrey-Hamel flow with heat and mass transfer characteristics of Jeffrey Nanofluid in a diverging-Converging Channel, Results Chem. 18 (2025) 102725. https://doi.org/10.1016/j.rechem.2025.102725.
[43] A. Wakif, Numerical simulation of MHD Sakiadis flows of convectively heated thixotropic nanofluids in a porous medium using revised transport laws and Wakif-Buongiorno's model, Partial Differ. Equ. Appl. Math. 13 (2025) 101071. https://doi.org/10.1016/j.padiff.2024.101071.
[44] S.E. Ahmed, Z.Z. Rashed, MHD natural convection in a heat generating porous medium-filled wavy enclosures using Buongiorno's nanofluid model, Case Stud. Therm. Eng. 14 (2019) 100430. https://doi.org/10.1016/j.csite.2019.100430.
[45] S. Yekani Motlagh, S. Taghizadeh, H. Soltanipour, Natural convection heat transfer in an inclined square enclosure filled with a porous medium saturated by nanofluid using Buongiorno's mathematical model, Adv. Powder Technol. 27 (2016) 2526–2540. https://doi.org/10.1016/j.apt.2016.09.016.
[46] L. Tham, R. Nazar, I. Pop, Mixed convection flow from a horizontal circular cylinder embedded in a porous medium filled by a nanofluid: Buongiorno–Darcy model, Int. J. Therm. Sci. 84 (2014) 21–33. https://doi.org/10.1016/j.ijthermalsci.2014.04.020.
[47] H. Alrabaiah, S. Iftikhar, A. Saeed, M. Bilal, S.M. Eldin, A.M. Galal, Numerical calculation of Darcy Forchheimer radiative hybrid nanofluid flow across a curved slippery surface, South Afr. J. Chem. Eng. 45 (2023) 172–181. https://doi.org/10.1016/j.sajce.2023.05.013.
[48] S. Dero, H. Shaikh, G.H. Talpur, I. Khan, S.O. Alharbim, M. Andualem, Influence of a Darcy-Forchheimer porous medium on the flow of a radiative magnetized rotating hybrid nanofluid over a shrinking surface, Sci. Rep. 11 (2021) 24257. https://doi.org/10.1038/s41598-021-03470-x.
[49] S.A. Mathias, K.N. Moutsopoulos, Approximate solutions for Forchheimer flow during water injection and water production in an unconfined aquifer, J. Hydrol. 538 (2016). https://doi.org/10.1016/j.jhydrol.2016.03.048.
[50] A.D. Koussis, K. Mazi, F. Riou, G. Destouni, A correction for Dupuit–Forchheimer interface flow models of seawater intrusion in unconfined coastal aquifers, J. Hydrol. 525 (2015) 277–285. https://doi.org/10.1016/j.jhydrol.2015.03.047.
[51] P. Srivastava, P. Kumar Yadav, Brinkman-Forchheimer model for unsteady mixed convective magnetohydrodynamics flow of couple stress fluid through swarm of particles at high magnetic Reynold number: Cell model technique, Chem. Eng. Sci. 321 (2026) 122758. https://doi.org/10.1016/j.ces.2025.122758.
[52] Q. Wang, H. Zhan, Y. Wang, Single-well push-pull test in transient Forchheimer flow field, J. Hydrol. 549 (2017) 125–132. https://doi.org/10.1016/j.jhydrol.2017.03.066.
[53] P. Jangid, A. Pandey, D. Tripathi, K. Sharma, Darcy–Forchheimer flow driven by membrane pumping and magnetohydrodynamics: perturbation solution, Chin. J. Phys. 96 (2025) 1435–1452. https://doi.org/10.1016/j.cjph.2025.06.004.
[54] M. Rashid, M. Irfan, T. Muhammad, A. Abu-Jrai, M.S. Anwar, Dynamics of solar radiation absorption for Darcy-Forchheimer Carreau nanofluid considering variable conductivity with chemical reaction: A solar thermal energy application, Results Eng. 26 (2025) 104670. https://doi.org/10.1016/j.rineng.2025.104670.
[55] H.I. Hussein, A.A. Darem, A.A. Alhashmi, N. Nazarova, J. Younis, M. Abbas, H.A. Garalleh, A. Alalawi, Design of artificial neural networks for darcy-forchheimer flow of boger hybrid nanofluid with CattaneoChristov theory: Thermofluidic applications, Int. J. Thermofluids 30 (2025) 101473. https://doi.org/10.1016/j.ijft.2025.101473.
[56] B.K. Sharma, A. Kumar, B. Almohsen, U. Fernandez-Gamiz, Computational analysis of radiative heat transfer due to rotating tube in parabolic trough solar collectors with Darcy Forchheimer porous medium, Case Stud. Therm. Eng. 51 (2023) 103642. https://doi.org/10.1016/j.csite.2023.103642.
[57] A. Shafiq, A.B. Çolak, T.N. Sindhu, Comparative analysis to study the Darcy–Forchheimer Tangent hyperbolic flow towards cylindrical surface using artificial neural network: An application to Parabolic Trough Solar Collector, Math. Comput. Simul. 216 (2024) 213–230. https://doi.org/10.1016/j.matcom.2023.09.014.

[58] A. Eladeb, A. Sambas, M. Bilal, B.M. Alshammari, L. Kolsi, Radiative Darcy-Forchheimer hybrid nanofluid flow with thermal and bioconvection impacts over a stretching/shrinking sheet, J. Radiat. Res. Appl. Sci. 18 (2025) 101266. https://doi.org/10.1016/j.jrras.2024.101266.
[59] S.A. Lone, A. Khan, H. Alrabaiah, S. Shahab, Z. Raizah, I. Ali, Dufour and Soret diffusions phenomena for the chemically reactive MHD viscous fluid flow across a stretching sheet with variable properties, Int. J. Heat Fluid Flow 107 (2024) 109352. https://doi.org/10.1016/j.ijheatfluidflow.2024.109352.
[60] H. Arafat, A. Anjum, S.S. Zafar, M.F. Ahmed, F. Ali, A.M. Saeed, H.O. Sidi, D.M. Khidhi, N.A. Shah, Entropy generation in radiative bioconvective Maxwell nanofluid flow influenced by Lorentz force and Darcy–Forchheimer porous rotating disk, J. Radiat. Res. Appl. Sci. 18 (2025) 101993. https://doi.org/10.1016/j.jrras.2025.101993.
[61] M.I. Khan, F. Alzahrani, A. Hobiny, Simulation and modeling of second order velocity slip flow of micropolar ferrofluid with Darcy–Forchheimer porous medium, J. Mater. Res. Technol. 9 (2020) 7335–7340. https://doi.org/10.1016/j.jmrt.2020.04.079.
[62] G. Rasool, A. Shafiq, C.M. Khalique, T. Zhang, Magnetohydrodynamic Darcy-Forchheimer nanofluid flow over a nonlinear stretching sheet, Phys. Scr. 94 (2019) 105221. https://doi.org/10.1088/1402-4896/ab18c8.
[63] F. Ali, A. Zaib, B.S. Abdullaeva, R. Altuijri, M.I. Khan, Darcy Forchheimer flow of terny hybrid nanofluid flow through a blood circulation respiratory system, Colloid Polym. Sci. 301 (2023) 1247–1259. https://doi.org/10.1007/s00396-023-05138-6.
[64] H. Gul, M. Ramzan, C.A. Saleel, S. Kadry, A comparative analysis of ternary-hybrid nanofluid flows through a stretching cylinder influenced by an induced magnetic field with homogeneous-heterogeneous reactions, Numer. Heat Transf. Part - Appl. 86 (2025) 1688–1703. https://doi.org/10.1080/10407782.2023.2281543.
[65] M.F. Endalew, X. Zhang, Analysis of Navier slip effects in ionized power-law hybrid nanofluid flow through a Darcy–Forchheimer porous medium with modified Fourier heat transfer, Partial Differ. Equ. Appl. Math. 16 (2025) 101299. https://doi.org/10.1016/j.padiff.2025.101299.
[66] A.S. Mittal, V. Kori, MHD micropolar nanofluid flow and heat transfer over a stretching sheet in Darcy–Forchheimer porous media with active and passive control mechanisms, Therm. Adv. 5 (2025) 100080. https://doi.org/10.1016/j.thradv.2025.100080.
[67] N.I. Ghoneim, A.M. Amer, K.S.M. AL-Saidi, A.M. Megahed, Physical characteristics due to activation energy of dissipative heat transfer in Reiner–Philippoff nanofluid with Darcy–Forchheimer model, Case Stud. Therm. Eng. 61 (2024) 105059. https://doi.org/10.1016/j.csite.2024.105059.
[68] Z.H. Khan, O.D. Makinde, A. Trounev, W.A. Khan, R. Ahmad, Entropy generation and heat transfer in Time-Fractional mixed convection of nanofluids in Darcy-Forchheimer porous channel, Eng. Sci. Technol. Int. J. 60 (2024) 101908. https://doi.org/10.1016/j.jestch.2024.101908.
[69] T. Shahzad, S. Munir, T. Salahuddin, M. Awais, Numerical insights of heat and mass transfer in a Darcy-Forchheimer porous space subjected to MHD dissipative stagnation point flow of cross nanofluid towards a melting stretching cylindrical surface, Int. Commun. Heat Mass Transf. 159 (2024) 108088. https://doi.org/10.1016/j.icheatmasstransfer.2024.108088.
[70] N. Khemiri, S. Rehman, T. Saidani, V. Tirth, Heat transfer analysis of radiated thin-film flow of couple-stress nanofluid embedded in a Darcy-Forchheimer medium with Newtonian heating effects, Nucl. Eng. Technol. 57 (2025) 103510. https://doi.org/10.1016/j.net.2025.103510.
[71] M.A. Memon, K. Jacob, H.B. Lanjwani, E.E. Mahmoud, Darcy-Forchheimer MHD micropolar water based hybrid nanofluid flow, heat and mass transfer features past on stretching/shrinking surface with slip and radiation effects, Results Eng. 23 (2024) 102534. https://doi.org/10.1016/j.rineng.2024.102534.
[72] M. Kaviany, Principles of Heat Transfer in Porous Media, Springer US, New York, NY, 1991. https://doi.org/10.1007/978-1-4684-0412-8.
[73] E. Michaelides, Nanofluidics: Thermodynamic and Transport Properties, 1st ed., Springer International Publishing, Cham, 2014. https://doi.org/10.1007/978-3-319-05621-0.
[74] H.K. Dawood, H.A. Mohammed, K.M. Munisamy, Heat transfer augmentation using nanofluids in an elliptic annulus with constant heat flux boundary condition, Case Stud. Therm. Eng. 4 (2014) 32–41. https://doi.org/10.1016/j.csite.2014.06.001.
[75] E.J. Wasp, J.P. Kenny, R.L. Gandhi, Solid-liquid Flow Slurry Pipeline Transportation, Trans Tech Publications, 1977.
[76] Y. Xuan, W. Roetzel, Conceptions for heat transfer correlation of nanofluids, Int. J. Heat Mass Transf. 43 (2000) 3701–3707. https://doi.org/10.1016/S0017-9310(99)00369-5.
[77] D.A. Nield, A. Bejan, Convection in Porous Media, Springer, New York, NY, 2013. https://doi.org/10.1007/978-1-4614-5541-7.
[78] R.S. Vajjha, D.K. Das, Specific Heat Measurement of Three Nanofluids and Development of New Correlations, J. Heat Transf. 131 (2009). https://doi.org/10.1115/1.3090813.

[79] S.A. Angayarkanni, J. Philip, Review on thermal properties of nanofluids: Recent developments, Adv. Colloid Interface Sci. 225 (2015) 146–176. https://doi.org/10.1016/j.cis.2015.08.014.
[80] H.C. Brinkman, The Viscosity of Concentrated Suspensions and Solutions, J. Chem. Phys. 20 (1952) 571–571. https://doi.org/10.1063/1.1700493.
[81] F.P. Incropera, D.P. DeWitt, T.L. Bergman, A.S. Lavine, Introduction to Heat Transfer, Wiley, 2006.
[82] D. Pal, G. Mandal, Magnetohydrodynamic stagnation-point flow of Sisko nanofluid over a stretching sheet with suction, Propuls. Power Res. 9 (2020) 408–422. https://doi.org/10.1016/j.jppr.2020.06.002.
[83] H. Fazeli, S. Madani, P. Rahim Mashaei, Nanofluid forced convection in entrance region of a baffled channel considering nanoparticle migration, Appl. Therm. Eng. 106 (2016) 293–306. https://doi.org/10.1016/j.applthermaleng.2016.06.010.
[84] C.J.M. Lasance, The Thermal Conductivity of Silicon Dioxide, Electron. Cool. (2004). https://www.electronics-cooling.com/2004/08/the-thermal-conductivity-of-silicon-dioxide/ (accessed February 15, 2026).
[85] K. Khanafer, K. Vafai, M. Lightstone, Buoyancy-driven heat transfer enhancement in a two-dimensional enclosure utilizing nanofluids, Int. J. Heat Mass Transf. 46 (2003) 3639–3653. https://doi.org/10.1016/S0017-9310(03)00156-X.
[86] S.K. Das, N. Putra, P. Thiesen, W. Roetzel, Temperature Dependence of Thermal Conductivity Enhancement for Nanofluids, J. Heat Transf. 125 (2003) 567–574. https://doi.org/10.1115/1.1571080.
[87] P.J. Pritchard, J.W. Mitchell, Fox and McDonald's Introduction to Fluid Mechanics, John Wiley & Sons, 2016.

Supplementary Files

This is a list of supplementary files associated with this preprint. Click to download.

- Graphicalabstract.docx